Two Dimensional Scattering Analysis of Data-Linked Support Strings for Bistatic Measurement Systems

THESIS

William Keichel, Captain, USAF

AFIT/GE/ENG/09-24

DEPARTMENT OF THE AIR FORCE
AIR UNIVERSITY

AIR FORCE INSTITUTE OF TECHNOLOGY

Wright-Patterson Air Force Base, Ohio

The views expressed in this thesis are those of the author and do not reflect the official policy or position of the United States Air Force, Department of Defense, or the United States Government.

AFIT/GE/ENG/09-24

Two Dimensional Scattering Analysis of Data-Linked Support Strings for Bistatic Measurement Systems

THESIS

Presented to the Faculty

Department of Electrical and Computer Engineering

Graduate School of Engineering and Management

Air Force Institute of Technology

Air University

Air Education and Training Command

In Partial Fulfillment of the Requirements for the

Degree of Master of Science in Electrical Engineering

William Keichel, B.S.E.E.

Captain, USAF

March 2009

AFIT/GE/ENG/09-24

Two Dimensional Scattering Analysis of Data-Linked Support Strings for Bistatic Measurement Systems

William Keichel, B.S.E.E.
Captain, USAF

Approved:

/signed/	19 Mar 2009
Dr. Peter J. Collins (Chairman)	date
/signed/	19 Mar 2009
Dr. Michael J. Havrilla (Member)	date
/signed/	19 Mar 2009
Maj. Michael A. Saville (Member)	date

AFIT/GE/ENG/09-24

Abstract

Use of data-linked strings to support a bistatic antenna is being considered as a possible improvement to indoor bistatic radar cross section measurement systems. Analysis of candidate data-linked strings is required to understand the potential clutter contribution posed by such a system. The main objective of this research is to determine the scattering properties of four data-linked support string samples. Another goal is to determine the material properties of the string material through nondestructive means if possible. The final goal is to model the samples as a single wire coated with a dielectric material and determine the validity of the model. To meet these goals, the two dimensional radar cross section of each sample is measured with a focused beam system. The resulting measurements are used in conjunction with an analytic model of a dielectric-coated wire to estimate the material properties of the string material. Finally, a dielectric-coated wire model for each sample is analyzed using COMSOL Multiphysics software, and the results are compared with the measured two dimensional radar cross section. As a result of this study, the two dimensional radar cross section of each sample is presented for both vertical and horizontal polarizations. Also, the effective relative permittivity of each string sample is found and used in the COMSOL model. The COMSOL models are shown to be relatively accurate representations of the string samples.

Acknowledgements

I dedicate this thesis to Lt Matt "Tao" Williams, my friend, mentor, and brother. May you rest in peace. When I began my Air Force career as an electronic warfare systems specialist, I could not imagine being where I am today. The Air Force has enabled me to realize a potential I did not know existed within myself. I want to acknowledge the people who I worked with throughout my career and shared experiences with that shaped me into who I am today. As for my AFIT experience, I could not have completed this thesis without the cumulative support from numerous people. I would like to acknowledge my thesis committee. To Dr. Peter Collins, thank you for your steadfast faith I would finish on time even when I thought all was lost. To Dr. Michael Havrilla, thank you for your seemingly endless energy explaining the physical insight over and over until I understood even while you were recovering. To Maj Michael Saville, thank you for stepping up when Dr. Havrilla was unavailable. A special thanks to Capt Milo Hyde for helping troubleshoot a problem with the analytic model and preventing additional down time when time was a commodity I could not afford to lose. I would also like to acknowledge my AFIT LO peers, we could not have done this alone. Finally, I am most grateful for the unending support and love from my wife and children without which this was not possible. I love you.

William Keichel

Table of Contents

Page

List of Figures

List of Tables

List of Abbreviations

Two Dimensional Scattering Analysis of Data-Linked Support Strings for Bistatic Measurement Systems

I. Introduction

The main objective of this research is to determine the scattering properties of four data-linked support string samples. Another goal is to determine the material properties of the string material through nondestructive means if possible. The final goal is to model the samples as a single wire coated with a dielectric material and determine the validity of the model. The following section provides the motivation behind these goals.

1.1 Motivation

The radar cross section (RCS) is an important property of an aircraft. Understanding the scattering mechanisms associated with aircraft RCS analysis is essential to low observable engineers. Only after understanding the contributions of aircraft features and materials, can low observable engineers seek to mitigate these contributions through RCS reduction techniques. These techniques include aircraft feature shaping and material coating. The importance of RCS reduction is realized in increased survivability and effectiveness of military aircraft in hostile environments. Hostile environments contain surveillance radars to detect aircraft and alert airborne interceptors equipped with radar guided air-to-air missiles. In addition to the airborne threat, the environment includes surface threats such as anti-aircraft artillery (AAA) and surface-to-air missile (SAM) systems. Both use radar to acquire and track the aircraft before engaging. In the case of the AAA system, the targets position, velocity, and direction are used to aim the guns. SAM systems use the radar to either guide the missile from launch until intercept, illuminate the aircraft for a semi-active missile to guide itself to intercept, or guide an active missile close enough for the missile to use its own radar to track and intercept the aircraft. How effective these

threats are against aircraft, in part depends on the RCS of the aircraft. Significant resources are put into knowing the RCS of aircraft because of this dependence.

There are two types of RCS measurement facilities, outdoor ranges and indoor anechoic chambers [12]. Outdoor ranges are necessary for measuring large targets which require significant distance between the radar and the target to satisfy the far-field condition, the distance between the two must be greater than $\frac{2D^2}{\lambda}$ where D is the largest dimension of the target and λ is the free-space wavelength of the electromagnetic (EM) wave [16]. Outdoor ranges are susceptible to adverse weather conditions, unavoidable clutter interaction, and scene uncertainties like clutter motion from wind or wildlife. Anechoic chambers provide a more controlled and stable environment to measure RCS. Because they are indoors, their size limitations reduce the size of targets that can be measured in order to meet the far-field requirements. In order to measure low RCS targets in an anechoic chamber, the chamber clutter is reduced by adding radar absorbing material (RAM) to attenuate reflections from the walls, floor, and ceiling. According to Blacksmith, The Ohio State University was probably first in designing an anechoic room capable of measuring small RCS targets [6]. Traditionally, targets are mounted on a support pylon with the ability to rotate the target. This enables RCS vs. angle and frequency measurements. However, error is introduced into the measurements due to target and support interaction. As the target RCS gets lower and the measurement systems improve, this interaction can contaminate the measurement with error [7]. One method to mitigate this error is through signal processing techniques [8]. Another method involves designing a better support system to reduce interaction. A string support system is such a system. There are still interactions between the target and strings [9], [26], but it is an overall improvement to the measurement system. Figure 1.1 shows an example string system used in the Air Force Institute of Technology (AFIT) anechoic chamber.

Figure 1.2 shows two radar scenarios, a monostatic radar and a bistatic radar. As the figure depicts, a monostatic radar refers to the transmit and receive antenna being colocated, and a bistatic radar has the two antennas separated. Because the ma-

(a) (b)

Figure 1.1: AFIT range string support system.

jority of threats use a monostatic radar configuration, the emphasis has been put on measuring the monostatic RCS. With the success of stealth technology against monostatic systems, the possibility of using a bistatic radar configuration as a counter-stealth technique is a concern [27]. This has increased the interest in bistatic RCS measurements. Bistatic radars are not a new concept. Until the invention of the duplexer in 1936, which enabled a single antenna to both transmit and receive, early radars were bistatic out of necessity to provide enough isolation between the two antennas [13]. In addition to measuring the bistatic RCS to simply know the RCS at a specific bistatic angle, bistatic RCS analysis can aid in bistatic RCS reduction techniques [24]. A bistatic measurement system can be used in the AFIT range and is pictured in Figure 1.3. This is a good system for measuring the bistatic RCS of objects. However it is obvious from the picture, the entire bistatic apparatus is a clutter contributor. Another contributor is the bare floor required for moving the bistatic arm. This may not be a problem with measuring common targets, but it may be problematic for measuring low RCS objects. Just as the support string system improves monostatic RCS measurements by removing the target pylon, it may be possible to improve the bistatic measurements by replacing the bistatic antenna support apparatus with a string sup-

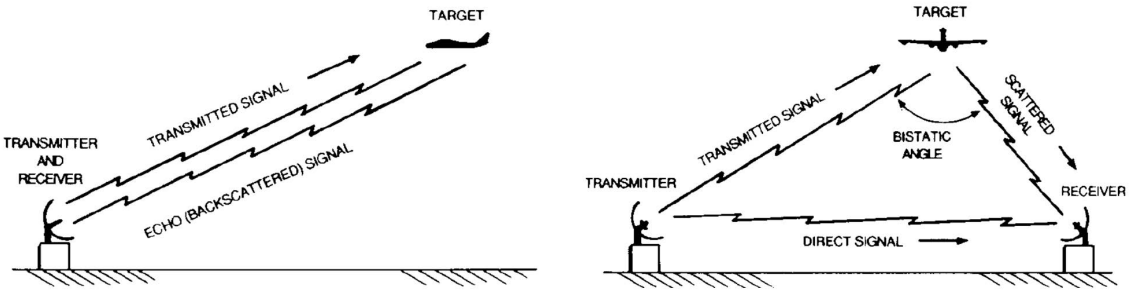

(a) (b)

Figure 1.2: Diagrams of (a) monostatic radar and (b) bistatic radar [13].

port system. Using a string system to support the bistatic antenna has challenges to overcome not experienced with the target string support system which only needs to support the target. A main challenge is accommodating the radio frequency (RF) cable which feeds the received RF to the receiver for measurement. Because it is a shielded coaxial cable, its clutter contribution is significantly more than the expected contributions of the support strings. Also, RF cables have loss that attenuates the measured signal. The signal loss can be significant for long cables. The cable length required for a bistatic antenna string support system may require in-line amplification which can introduce noise into the measurement. The RF cable may be removed by mounting a receiver at the back-end of the antenna or converting the measured RF to a digital signal. Although the RF cable would be gone, these options require power and a data link. The data link may be a wire or a fiber optic (FO) cable depending on the configuration.

1.2 Objectives

The Air Force Research Laboratory (AFRL) Sensors Directorate Signature Division has a Stewart Support String System for target support in their Advanced Compact Range. To explore the possibility of a data-linked string supported bistatic

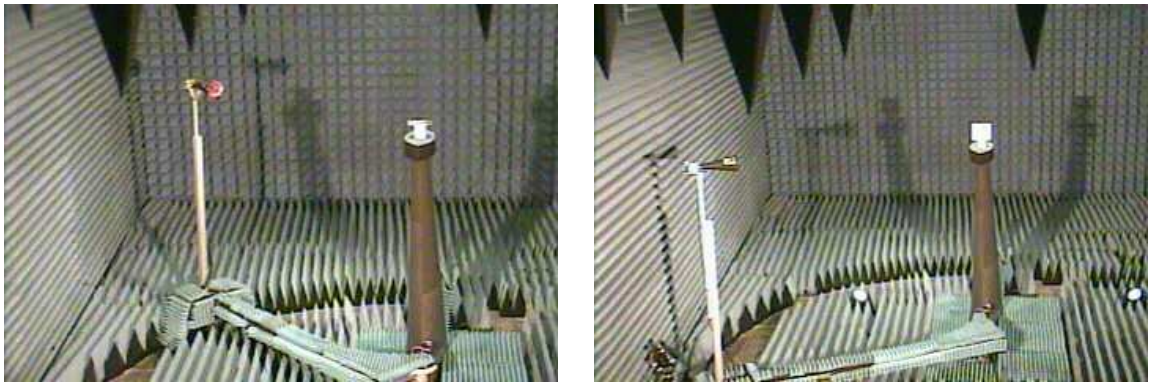

(a) (b)

Figure 1.3: AFIT range bistatic arm.

antenna, they have provided some sample data-linked support strings for analysis. This research effort is required as an initial step in designing a bistatic antenna string support system, a design that minimizes the clutter contribution of the bistatic antenna support system. The clutter contribution of the data-linked string may be a function of the type of string, the number of wires contained in the string, and whether the string contains FO cables. This study attempts to provide some insight to these factors by asking the following questions:

1. Given some samples, what is the clutter contribution of each sample?
2. Can accurate scattering analysis be performed with a focus beam system?
3. What are the scattering mechanisms associated with the samples?
4. Can the constitutive parameters of the samples be determined through non-destructive evaluation?
5. Can the strings be accurately modeled as a single wire with a dielectric coating for numerical analysis?

The rest of this thesis is broken up into four chapters. Chapter 2 provides a background for the analysis. Chapter 3 details the procedures of the analysis. Chapter 4 provides the results with explanation. Finally, chapter 5 summarizes the thesis and provides potential future research direction.

II. Background

The clutter contribution of the data-linked support strings can be characterized by their scattering properties. The samples can be described as dielectric-coated wires. A wire is a conducting cylinder with a very small radius relative to wavelength. Scattering analysis of dielectric-coated conducting cylinders is not new and has been explored by many including [15], [10], [20], [21], and [23]. However, their analysis considers a single conducting cylinder clad with a dielectric layer of uniform thickness. The data-linked support strings contain multiple wires of varying radii and some also contain FO cables. In addition, the string material is not exactly a uniform dielectric.

This chapter provides the necessary background for the research effort. It includes the definition of radar cross section as it applies to scattering analysis. Also, the concept of the two dimensional (2D) RCS is introduced. The Georgia Tech Research Institute (GTRI) focus beam system is able to simulate a 2D RCS measurement environment. A section is included to provide details about the focus beam system. The analytic model of a perfect electric conductor (PEC) cylinder needed for RCS correction is derived in the analytic model section. The analytic model section also contains the derivation of dielectric-coated PEC cylinder model. Finally, the benefits of a numerical model is described.

2.1 Radar Cross Section

Scattering, as related to electromagnetics, is a phenomena associated with a structure in the path of a propagating EM wave. The incident wave induces currents on the surface of the structure which in turn radiate EM energy in different directions as a scattered field. According to Knott, the resulting scattered field's spatial distribution depends on "the size, shape, and composition of the object and on the waveform and direction of arrival of the incident wave" [16]. It is because of scattering, radars can detect aircraft. For low observable engineers, understanding how objects scatter EM energy is essential. This leads to an entire community dedicated to scattering analysis. The results of the analysis are useful for scattering predictions

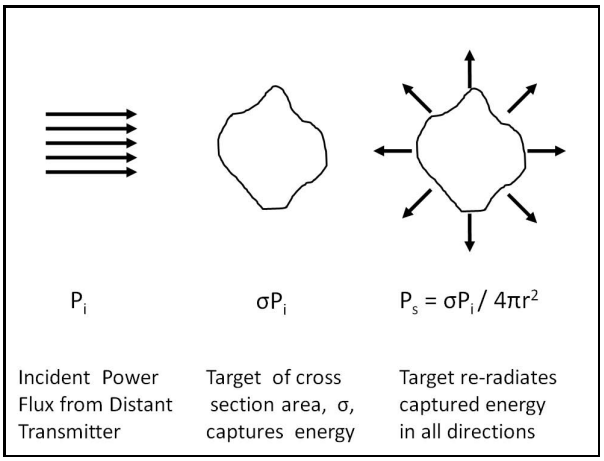

Figure 2.1: Illustration of RCS derivation [16].

of complex structures and materials. RCS prediction is fundamental to design and development of stealth platforms.

A characterization of an object as a function of the scattered energy is the RCS represented by σ. The IEEE defines RCS as "a measure of reflective strength of a target defined as 4π times the ratio of the power per unit solid angle scattered in a specified direction to the power per unit area in a plane wave incident on the scatterer from a specified direction" [16]. Mathematically, it is the limit of that ratio as the distance between the scatterer and observer approaches infinity. The limit ensures the RCS is a far-field quantity and is independent of distance. In equation form it is,

$$\sigma = \lim_{r \to \infty} \left[4\pi r^2 \frac{|\mathbf{E}^s|^2}{|\mathbf{E}^i|^2} \right] \tag{2.1}$$

where r is the distance from the scatterer to the observer, and the scattered and incident electric fields are $\mathbf{E}^s$ and $\mathbf{E}^i$ respectively.

The following is how Knott intuitively derives the RCS equation [16]. Figure 2.1 illustrates the derivation. The incident power density from a radar at a scatterer is P_i ($\frac{\mathrm{W}}{\mathrm{m}^2}$). The cross sectional area of the target, σ (m^2), relates to the amount of power intercepted by the target through the product of the two, σP_i (W). It is assumed the

power intercepted is re-radiated as scattered power uniformly in all 4π steradians (sr) of space. The scattered power density is now given by

$$P_s = \frac{\sigma P_i}{4\pi R^2} \left(\frac{\mathrm{W}}{\mathrm{m}^2} \right) \tag{2.2}$$

Solving equation (2.2) for σ gives

$$\sigma = 4\pi R^2 \frac{P_s}{P_i} \left(\mathrm{m}^2 \right) \tag{2.3}$$

where R is the distance from the scatterer and is far enough to satisfy the far-field criterion. As described, Knott shows the RCS is a ratio of the scattered power density to the incident power density. The power of an EM wave is proportional to the square of the magnetic or electric field. As in equation (2.1), the RCS can be expressed in terms of the incident and scattered electric, **E**, or magnetic, **H**, fields. Some factors that affect a target's measured RCS are

- position of the transmit antenna relative to the target
- position of the receive antenna relative to the target
- target geometry and composition
- angular orientation of the target relative to the antennas
- frequency of the transmitted EM wave

The RCS is usually represented in units of decibels per square meter (dBsm). It is an important characteristic of a target and is measured for a number of reasons [16]. The reasons that relate to this thesis are: acquire understanding of basic scattering phenomena, acquire diagnostic data, and verify system performance. Since the RCS is a function of the scattered field and the scattered field is a function of the scatterer, the RCS contains information about the scatterer. This makes measuring the RCS of the data-linked string samples integral to this thesis.

2.2 Two Dimensional RCS

Since all objects are three dimensional (3D) the RCS described in the previous section is the 3D RCS, σ_{3D}. An academic exercise is calculating the RCS of a 2D target. If the target is assumed to be infinitely long and does not vary in shape or composition along one dimension, z, it is considered z-invariant. A z-invariant target is defined by its 2D cross sectional construction in the x-y plane at $z = 0$ and is the same for all z. Some targets considered z-invariant are infinitely long wires, cylinders and wedges. Scattering analysis of such targets only makes sense if the incident field is propagating parallel to the x-y plane. Such fields are described by the orientation of either the incident magnetic field, $\mathbf{H}^i$, or electric field, $\mathbf{E}^i$, with respect to the z axis. When $\mathbf{H}^i$ is oriented orthogonal to the z axis, the incident wave is labeled transverse magnetic field with respect to the z axis or TM^z. Conversely, a transverse electric field with respect to the z axis, TE^z, is the label for an incident wave with the electric field orthogonal to the z-axis. For the TM^z case, the incident electric field has only a $\hat{z}$ component, E_z^i. The resulting scattered electric field will only consist of a $\hat{z}$ component, E_z^s. This is also true for the TE^z case, where H_z^i and H_z^s are the scalar fields. 2D targets only need to be analyzed at $z = 0$. This is because the contributions of the positive z and negative z cancel each other [1].

The same assumption exists for the 2D RCS as with the 3D RCS. The antenna and target are far enough away from each other to satisfy the far-field criterion. However instead of the waves spreading spherically from the antenna and the target, they spread cylindrically. Equation (2.4) is the mathematical definition of the 2D RCS, σ_{2D},

$$\sigma_{2D} = \lim_{\rho \to \infty} \left[2\pi\rho \frac{|\mathbf{E}^s|^2}{|\mathbf{E}^i|^2} \right] \tag{2.4}$$

where ρ is the distance from the scatterer to the observer. The 2D RCS is represented in units of decibels per meter (dBm).

Since the targets being considered for this thesis are long data-linked strings, they are good candidates for 2D RCS analysis. A system designed to measure reflection and transmission coefficients of materials, but is also capable of measuring the 2D RCS of a target is the GTRI focus beam system.

2.3 GTRI Focus Beam System

The GTRI focus beam measurement system is designed to make free-space measurements to find the reflection and transmission coefficients of materials [1]. By doing so, the material properties, permittivity and permeability, can be calculated. These measurements require plane wave illumination. Recall the distance required to achieve planar waves is greater than $\frac{2D^2}{\lambda}$ where D is the largest dimension of the target. For a 0.5 m target and a frequency of 18 GHz, the distance between the antenna and the target should be greater than 30 m. The use of a microwave lens can reduce the required range [17]. To achieve plane waves in a compact distance, the GTRI focus beam system uses a collimating microwave lens to convert spherical waves from an antenna into a planar wave at the target. The collimating lens is convex on the antenna side and planar on the target side. The system must ensure the EM energy is confined to the material under test in order to reduce edge illumination which causes error. To achieve this, the system uses a focusing microwave lens to concentrate the majority of the energy within a "beamwaist". The focusing lens is planar on the antenna side and convex on the target side. The two lenses are placed together to combine the effects. This design can simulate 2D scattering analysis of targets by illuminating a z-invariant target-under-test with planar waves while keeping the edge illumination to a minimum by focusing the energy to the middle of the target. "The versatility of the measurement system for characterizing both constitutive and scattering properties distinguishes itself as an indispensable research and measurement tool" [1] making the focus beam system an ideal candidate tool for this thesis.

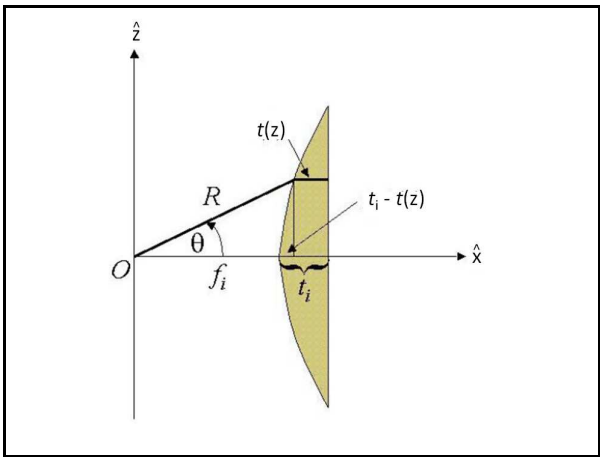

Figure 2.2: Focus beam system's collimating lens geometry [1].

2.3.1 Design Description. The following description is from the users guide provided with the GTRI focus beam system [1]. The collimating lens uses convex-plano geometry to convert the spherical waves emanating from the antenna into a plane wave. The lens consists of a material whose index of refraction and shape converts the spherical wave into a plane wave at the planar side of the lens using Snell's Law of Refraction, $n_1 \sin\theta_1 = n_2 \sin\theta_2$. This is referred to as geometric optics. Figure 2.2 illustrates the geometry of the system. Assuming the radiating antenna is a point source at the origin, the focal length, f_i, is the distance from the origin to the apex of the collimating lens. R is the distance from the origin to any point on the convex side of the lens. The lens is rotationally symmetric about the x *axis*. Therefore, the thickness of the lens, $t(z)$, is a function of the radius. The maximum thickness of the lens, t_i, is located at the x axis. The index of refraction, n, associated with the dielectric lens is assumed to have negligible electrical loss. The electrical distance from the origin to any point on the planar side of the lens must be equal. At zero degrees, the electrical length, EL, is

$$EL|_{\theta=0} = f_i + t_i n \ . \tag{2.5}$$

Equation (2.6) uses the Pythagorean Theorem to calculate the electrical length for $\theta \neq 0$,

$$EL|_{\theta \neq 0} = R + t(z)n = \sqrt{z^2 + \left[f_i + t_i - t(z)\right]^2} + t(z)n \ . \tag{2.6}$$

The shape of the lens as a function of f_i and n is found be equating equations (2.5) and (2.6) and solving for $t(z)$,

$$t(z) = t_i + \frac{f_i - \sqrt{f_i^2 + \left(\frac{n+1}{n-1}\right) z^2}}{n+1} \ . \tag{2.7}$$

Another way to express the lens shape as a function of n and f_i is

$$R(\theta) = \frac{f_i(n-1)}{n\cos(\theta) - 1} \left(\frac{\mathrm{m}}{\mathrm{deg}}\right) \tag{2.8}$$

which is a useful form when considering the antenna as something other than a point source.

No antenna is a point source. An antenna has a non-isotropic radiation pattern. The lens design takes this into account. The antenna radiation intensity, $U(\theta, \lambda)(\frac{\mathrm{W}}{\mathrm{sr}})$, is a function of angle and frequency. Assuming the spherical waves radiate from the origin as a function of the radiation intensity pattern, the differential power density at the convex side of the lens is the solid angle of a zone of a sphere times the radiation intensity. The geometry to find the differential radiation intensity is illustrated in Figure 2.3 (a). The solid angle of a zone of a sphere is,

$$S = \frac{2\pi Rh}{4\pi R^2} = \frac{1}{2}\sin(\theta)d\theta \ (\mathrm{sr}) \tag{2.9}$$

which can be used to find the power by multiplying the surface area by the radiation intensity pattern,

$$P(\theta, \lambda) = \frac{1}{2}U(\theta, \lambda)\sin(\theta)d\theta \ (\mathrm{W}) \ . \tag{2.10}$$

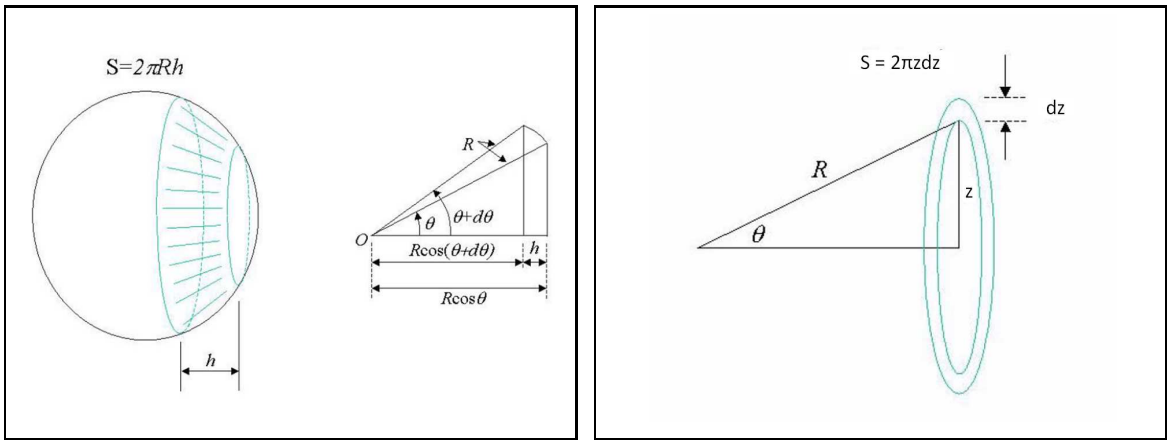

(a) (b)

Figure 2.3: (a) Differential radiation intensity of power entering the lens and (b) differential area of power leaving the lens [1].

The differential power collected by the convex side is related to the differential area of power on the planar side of the lens. Figure 2.3 (b) describes the geometry of the differential area of power leaving the collimating lens. The power profile is now a function of z and frequency and when multiplied by the differential area of the planar side of the lens is

$$2\pi z dz P(z,\lambda) \text{ (W)} . \tag{2.11}$$

Ideally, equations (2.15) and (2.11) are equal because the power collected by the lens should leave the lens. For this reason, the lens is assumed to be lossless. Setting them equal and solving for $P(z,\lambda)$, results in

$$P(z,\lambda) = \frac{U(\theta,\lambda)\sin(\theta)}{4\pi z\left(\frac{dz}{d\theta}\right)} \left(\frac{\text{W}}{\text{m}^2}\right) . \tag{2.12}$$

To express P in terms of frequency and angle, consider equation (2.8) and Figure 2.3 (b). The equation for z becomes

$$z = R\sin(\theta) = \frac{f_i(n-1)\sin(\theta)}{n\cos(\theta)-1}\left(\frac{\text{m}}{\text{deg}}\right) . \tag{2.13}$$

Letting

$$\frac{dz}{d\theta} = \frac{R(n - \cos(\theta))}{n\cos(\theta) - 1} \tag{2.14}$$

and substituting equations (2.14) and (2.13) in equation (2.12) makes P a function of angle instead of z,

$$P(\theta, \lambda) = \frac{U(\theta, \lambda)\sin(\theta)(n\cos(\theta) - 1)}{4\pi R^2 \sin(\theta)(n - \cos(\theta))} = \frac{(n\cos(\theta) - 1)^3}{(n-1)^2(n - \cos(\theta))}\frac{U(\theta, \lambda)}{4\pi f_i^2} \left(\frac{\mathrm{W}}{\mathrm{m}^2}\right) . \tag{2.15}$$

The radiation power density is normalized by dividing by $P(0, \lambda)$,

$$\frac{P(\theta, \lambda)}{P(0, \lambda)} = \frac{(n\cos(\theta) - 1)^3}{(n-1)^2(n - \cos(\theta))}\frac{U(\theta, \lambda)}{U(0, \lambda)} . \tag{2.16}$$

A directional antenna's maximum radiated power is at $\theta = 0$ which is known as the boresight of the antenna. Antennas are characterized by their 3 dB beamwidth, $\theta_{3\mathrm{dB}}$, where the power is one half the boresight power. The focusing lens uses Gaussian optics to focus the energy. Therefore, the geometric optics used to collimate the energy needs to be related to the Gaussian optics to focus the energy. This is done by assuming the field distribution of equation (2.16) is Gaussian and defined by

$$\exp\left(-2\frac{\theta_{3\mathrm{dB}}^2}{\theta_{1/e}^2}\right) = \frac{1}{2}\frac{(n\cos(\theta) - 1)^3}{(n-1)^2(n - \cos(\theta))} \tag{2.17}$$

where $\theta_{1/e}$ is the $1/e$ beamwidth and $\frac{U(\theta,\lambda)}{U(0,\lambda)} = \frac{1}{2}$. Solving for $\theta_{1/e}$ gives the $1/e$ beamwidth associated with Gaussian optics at the planar side of the collimating lens,

$$\theta_{1/e} = \theta_{3\mathrm{dB}}\sqrt{\frac{2}{-\ln\left[\frac{1}{2}\frac{(n\cos(\theta_{3\mathrm{dB}}) - 1)^3}{(n-1)^2(n - \cos(\theta_{3\mathrm{dB}}))}\right]}} . \tag{2.18}$$

Unlike antenna theory, Gaussian optics defines the beamwidth as the radius where the field (not power) is reduced by $1/e$ from the maximum on the axis of symmetry. The $1/e$ radius on the planar side of the focusing lens, w_L, is calculated

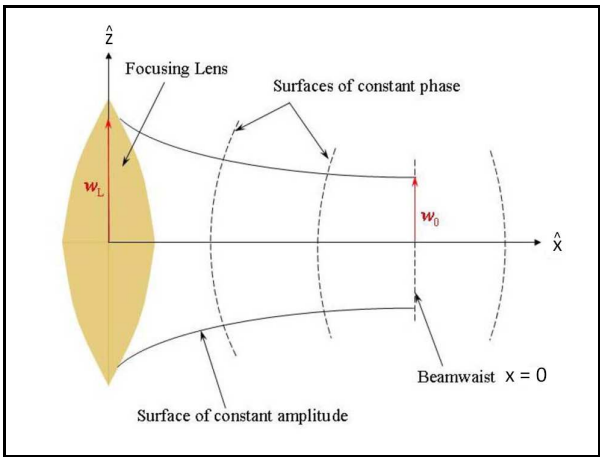

Figure 2.4: Focus beam system's focusing lens geometry [1].

as a function of $\theta_{1/e}$,

$$z(\theta_{1/e}) \equiv w_L = \frac{f_i(n-1)\sin(\theta_{1/e})}{n\cos(\theta_{1/e}) - 1} \tag{2.19}$$

where w_L is the $1/e$ radius at the planar side of the collimating lens. The radiated fields are now collimated at the planar side of the collimating lens and are ready to be focused by the focusing lens. The focusing lens produces a "quasi" plane-wave with a Gaussian amplitude taper at the target location. The focusing lens geometry is illustrated in Figure 2.4. The field radius, w_L, at the planar side of the focusing lens is focused down to the beamwaist, w_o, at the target location, $x = 0$. The Gaussian beam complex field distribution is characterized mathematically by equation (2.20) [1],

$$\Psi = A\frac{w_o}{w(x)}\exp\left(\frac{z^2}{w^2(x)}\right)\exp\left(-jkx\right)\exp\left(\frac{j\pi z^2}{\lambda C(x)}\right)\exp\left(j\arctan\left(\frac{\lambda x}{\pi w_o^2}\right)\right). \tag{2.20}$$

The surface of constant amplitude represent the $1/e$ beam radius along the x $axis$ as the fields propagate, $w(x)$, is defined by

$$w(x) = w_o\sqrt{1 + \left(\frac{\lambda x}{\pi w_o^2}\right)^2}. \tag{2.21}$$

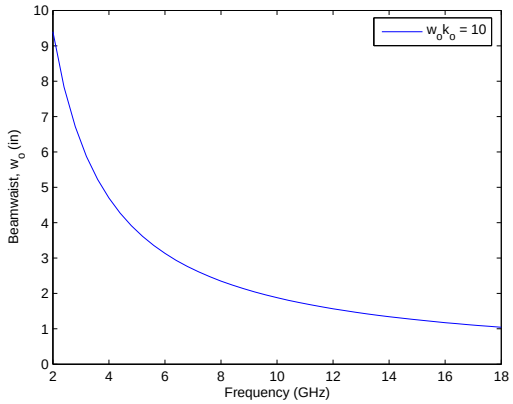

Figure 2.5: Beamwaist vs frequency for $w_o k_o = 10$.

The surfaces of constant phase represent the radius of curvature of the phase front, $C(x)$, along the x $axis$,

$$C(x) = x\left[1 + \left(\frac{\pi w_o^2}{\lambda x}\right)^2\right] \ . \tag{2.22}$$

Both parameters, $w(x)$ and $C(x)$, are functions of w_o. There is a limiting constraint associated with the focus beam system. The illuminating beam is based on Gaussian optics. A source of error is in assuming a plane wave illumination. The incident wave may be planar in phase but it is not in amplitude. To reduce the error to less than 1%, the beamwaist should satisfy the condition $k_o w_o \geq 10$ [22] where k_o is the free-space wave number ($\frac{2\pi}{\lambda}$). Solving for w_o,

$$w_o = \frac{10\lambda}{2\pi} \ , \tag{2.23}$$

gives the beamwaist as a function of frequency. Figure 2.5 shows the resulting beamwaist as a function of frequency. When used for measuring the constitutive parameters of materials, the focused beam system does not perform as well below 4 GHz [25]. Figure 2.6 is a visualization of the beam for 2 and 4 GHz. As the frequency increases, the focused beam becomes better defined in amplitude and phase. The effects at 2 GHz may cause errors in the 2D RCS measurement of the string samples.

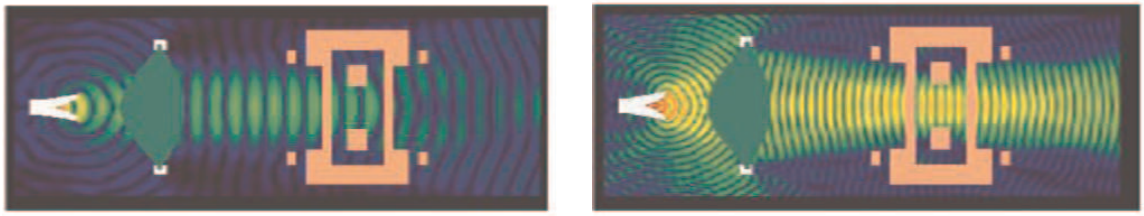

(a) (b)

Figure 2.6: Analysis of focus beam performance for (a) 2 GHz and (b) 4 GHz [11].

The GTRI focus beam system provides measured scattering analysis that can simulate 2D illumination of z-invariant targets. The measured data is not the 2D RCS. To obtain the 2D RCS, an analytic model is needed to generate the exact data of a reference target. The next section describes the analytic model.

2.4 Analytic Model

As seen in equation (2.2), the 2D RCS is a function of the magnitude ratio of the scattered and incident fields $\left(\frac{|\mathbf{E}^s|}{|\mathbf{E}^i|}, \frac{|\mathbf{H}^s|}{|\mathbf{H}^i|}\right)$. Since a dielectrically coated wire is being considered as a model for the data-linked string, the scattering solution for a circular cylinder is considered for this thesis. Since a circular cylinder is in the set of canonical shapes (square flat plate, triangle flat plate, dihedral, trihedral, sphere, etc.) which are building blocks of more complex structures, its scattering solution is explored by Balanis [5]. Chapter 11 of Balanis' text provides the foundation for the analytic model of a circular cylinder. Because it is intuitive plane waves will scatter cylindrically from cylindrical targets, it makes sense to consider cylindrical solutions to the vector wave equation [3]. The incident plane wave can also be represented cylindrically using a cylindrical wave transformation. Balanis shows a normalized

uniform plane wave propagating in the $\pm x$ direction can be written as

$$\mathbf{E} = \hat{z}E_z^{\pm} = \hat{z}e^{\pm j\beta x} = \hat{z}\sum_{n=-\infty}^{+\infty} j^{\mp n}J_n(\beta\rho)e^{jn\phi} \tag{2.24}$$

which contains an infinite sum of forward or reverse traveling cylindrical waves.

The analytic models required for this thesis are the PEC circular cylinder and the dielectric-coated PEC circular cylinder. The PEC model is for generating the exact data for the reference targets. The dielectric-coated PEC model represents the data-linked support string samples. The models are developed for both the TM^z and TE^z cases. The following sections show the derivation of the models from chapter 11 Balanis' text.

2.4.1 TM^z Case. For the TM^z case, the incident electric field consists only of a $\hat{z}$ component and the incident magnetic field consists only of a $\hat{y}$ component. The scattered electric field has only a $\hat{z}$ component as well. However, the scattered magnetic field has both $\hat{x}$ and $\hat{y}$ components. For this reason, it is convenient to use the electric field in the scattering model. The mathematical model of the incident field is represented in equation (2.25),

$$\mathbf{E}^i = \hat{z}E_z^i = \hat{z}E_o e^{-j\beta_o x} = \hat{z}E_o\sum_{n=-\infty}^{+\infty} j^{-n}J_n(\beta_o\rho)e^{jn\phi} \tag{2.25}$$

where the variable, E_o, is the amplitude of the incident wave and β_o is the free-space phase constant. The incident field is a propagating field or a traveling wave. Physically, cylindrical waves are expected to radiate from a cylinder after plane wave illumination. The scattered field is modeled as an infinite sum of outward traveling cylindrical waves,

$$\mathbf{E}^s = \hat{z}E_z^s = \hat{z}E_o\sum_{n=-\infty}^{+\infty} a_n H_n^{(2)}(\beta_o\rho)e^{jn\phi} \tag{2.26}$$

where a_n are amplitude coefficients that must be determined. The resulting magnitude ratio used to calculate the 2D RCS is

$$\frac{|\mathbf{E}^s|}{|\mathbf{E}^i|} = \frac{\left| E_o \sum_{n=-\infty}^{+\infty} a_n H_n^{(2)}(\beta_o \rho) e^{jn\phi} \right|}{|E_o e^{-j\beta_o x}|} \ . \tag{2.27}$$

Since RCS is a far-field characteristic, the argument of the Hankel function, $\beta_o\rho$, is very large and lends to the large argument approximation of the Hankel function,

$$H_n^{(2)}(\beta_o\rho) \overset{\beta_o\rho \to large}{\cong} \sqrt{\frac{2}{\pi\beta_o\rho}} e^{-(j\beta_o\rho - jn\frac{\pi}{2} - j\frac{\pi}{4})} \tag{2.28}$$

which can be written as

$$H_n^{(2)}(\beta_o\rho) \overset{\beta_o\rho \to large}{\cong} \sqrt{\frac{2}{\pi\beta_o\rho}} e^{-j\beta_o\rho} e^{jn\frac{\pi}{2}} e^{j\frac{\pi}{4}} \ . \tag{2.29}$$

Knowing $e^{j\frac{n\pi}{2}} = j^n$ *and* $e^{j\frac{\pi}{4}} = \sqrt{j}$, equation (2.29) can be simplified further as

$$H_n^{(2)}(\beta_o\rho) \overset{\beta_o\rho \to large}{\cong} j^n \frac{e^{-j\beta_o\rho}}{\sqrt{\rho}} \sqrt{\frac{2j}{\pi\beta_o}} \tag{2.30}$$

where $\dfrac{e^{-j\beta_o\rho}}{\sqrt{\rho}}$ is the Green's function for cylindrical waves in free space. Using the Hankel function large argument approximation, equation (2.27) becomes

$$\frac{|\mathbf{E}^s|}{|\mathbf{E}^i|} \overset{\beta_o\rho \to large}{\cong} \sqrt{\frac{2}{\pi\beta_o\rho}} \left| \sum_{n=-\infty}^{+\infty} j^n a_n e^{jn\phi} \right| \ . \tag{2.31}$$

The next step is to determine what a_n is for a specific scatterer. The PEC circular cylinder is considered first.

2.4.1.1 TM^z PEC Circular Cylinder. Before deriving a_n, the fields in the regions need to be defined. From Figure 2.7, there are two regions to consider. Region I is free-space outside the PEC cylinder ($\rho > a$). Region II is the PEC region

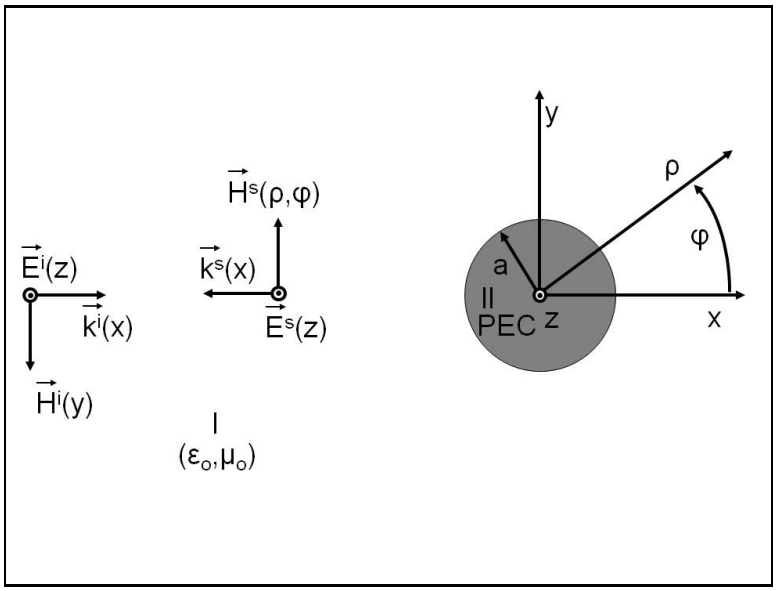

Figure 2.7: 2D PEC cylinder with TM^z illumination.

($\rho < a$). The total field of region I is the sum of the incident field and scattered field,

$$\mathbf{E}^t = \mathbf{E}^i + \mathbf{E}^s \ . \tag{2.32}$$

Since *region II* is a PEC, no fields exist in the region. To determine a_n, boundary conditions are applied. At the boundary of the PEC cylinder ($\rho = a$), the tangential component of the total field is zero [5].

$$\mathbf{E}^t = \hat{z}E_z^t(\rho = a, 0 \leq \phi \leq 2\pi, z) = 0 \tag{2.33}$$

Using equation (2.32) and substituting into equation (2.33), a_n can be solved for algebraically. By applying the orthogonal operator, $\frac{1}{2\pi}\int_{-\pi}^{\pi} e^{-jm\phi}\{\cdots\}d\phi$, to

$$\mathbf{E}^i + \mathbf{E}^s = \hat{z}E_o \sum_{n=-\infty}^{+\infty} \left[j^{-n}J_n(\beta_o a)e^{jn\phi} + a_n H_n^{(2)}(\beta_o a)e^{jn\phi}\right] = 0 \ , \tag{2.34}$$

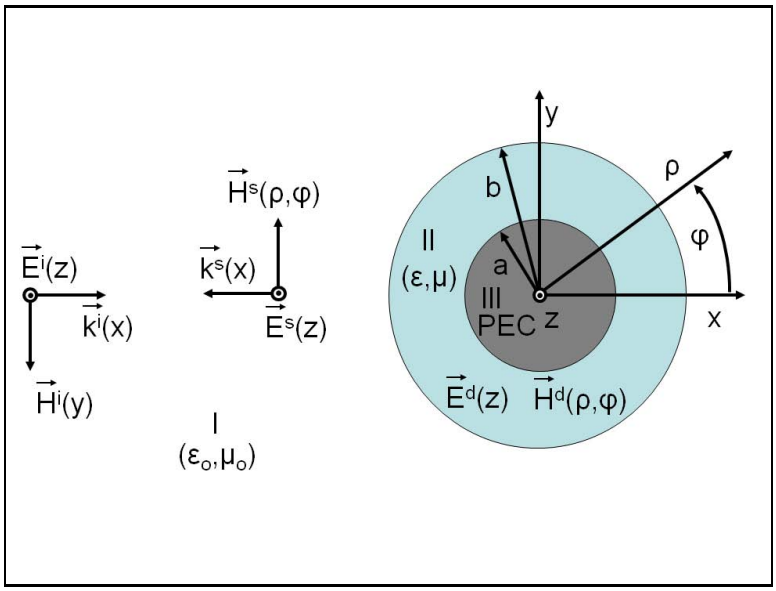

Figure 2.8: 2D dielectric-coated PEC cylinder with TM^z illumination.

equation (2.34) becomes

$$j^{-n}J_n(\beta_o a) + a_n H_n^{(2)}(\beta_o a) = 0 \ . \tag{2.35}$$

Solving for a_n results in

$$a_n = -j^{-n}\frac{J_n(\beta_o a)}{H_n^{(2)}(\beta_o a)} \ . \tag{2.36}$$

Substituting the solution for a_n into equation (2.31) gives the magnitude field ratio for a 2D PEC circular cylinder,

$$\frac{|\mathbf{E}^s|}{|\mathbf{E}^i|} \overset{\beta_o\rho\rightarrow large}{\cong} \sqrt{\frac{2}{\pi\beta_o\rho}}\left|\sum_{n=-\infty}^{+\infty}\frac{J_n(\beta_o a)}{H_n^{(2)}(\beta_o a)}e^{jn\phi}\right| \ . \tag{2.37}$$

The far-field TM^z 2D RCS of a PEC cylinder is found substituting equation (2.37) for the magnitude ration in equation (2.4).

2.4.1.2 TM^z Dielectric-Coated PEC Circular Cylinder. The dielectric-coated circular cylinder is considered in problem 11-27 in Balanis' text and solved

in the solution manual [5]. The solution manual provides the foundation for the dielectric-coated circular cylinder analytic model. Figure 2.8 illustrates the 2D dielectric-coated PEC cylinder geometry and the regions associated with it. As with the PEC case, region I is the free-space region surrounding the target ($\rho > b$). Region II is the dielectric region ($a < \rho < b$), and region III is the PEC region ($\rho < a$). The fields in region I are the same as the previous section defined by equations (2.25) and (2.26). The total electric field in region II is the dielectric electric field ($\mathbf{E}^d$). As stated before, the field inside the PEC is zero. The mathematical model for the dielectric electric field is

$$\mathbf{E}^d = \hat{z}E_z^d = \hat{z}E_o \sum_{n=-\infty}^{+\infty} \left[b_n J_n(\beta_d \rho) + c_n Y_n(\beta_d \rho)\right] e^{jn\phi} \tag{2.38}$$

where the sum of the Bessel and Neumann functions represent the field in the dielectric as a standing wave. The variable β_d is the phase constant of the dielectric. The amplitude coefficients are solved in the same manner as before, applying boundary conditions and enforcing continuity of tangential fields. At the PEC surface, $\rho = a$, the tangential components of the electric field is zero,

$$E_z^d|_{\rho=a} = 0 \ . \tag{2.39}$$

Setting equation (2.38) equal to zero and applying the orthogonal operator, $\frac{1}{2\pi}\int_{-\pi}^{\pi} e^{-jm\phi}\{\cdots\}d\phi$, equation (2.38) becomes

$$b_n J_n(\beta_d a) + c_n Y_n(\beta_d a) = 0 \ . \tag{2.40}$$

Solving for c_n algebraically provides c_n in terms of b_n,

$$c_n = -b_n \frac{J_n(\beta_d a)}{Y_n(\beta_d a)} \ . \tag{2.41}$$

At $\rho = b$, continuity is enforced by setting the tangential components of the total electric field in free space equal to the tangential components of the electric field in

the dielectric,

$$(E_z^i + E_z^s)|_{\rho=b} = E_z^d|_{\rho=b} \ . \tag{2.42}$$

Substituting for E_z^i, E_z^s, and E_z^d, equation (2.42) becomes

$$E_o \sum_{n=-\infty}^{+\infty} \left[j^{-n} J_n(\beta_o b) + a_n H_n^{(2)}(\beta_o b) \right] e^{jn\phi} = E_o \sum_{n=-\infty}^{+\infty} \left[b_n J_n(\beta_d b) + c_n Y_n(\beta_d b) \right] e^{jn\phi} \ . \tag{2.43}$$

After applying the orthogonal operator, $\frac{1}{2\pi}\int_{-\pi}^{\pi} e^{-jm\phi}\{\cdots\}d\phi$, equation (2.43) becomes,

$$j^{-n} J_n(\beta_o b) + a_n H_n^{(2)}(\beta_o b) = b_n J_n(\beta_d b) + c_n Y_n(\beta_d b) \ . \tag{2.44}$$

Substituting equation (2.41) for c_n and rearranging, equation (2.43) becomes

$$j^{-n} J_n(\beta_o b) + a_n H_n^{(2)}(\beta_o b) = b_n \left[\frac{J_n(\beta_d b) Y_n(\beta_d a) \ - \ J_n(\beta_d a) Y_n(\beta_d b)}{Y_n(\beta_d a)} \right] \tag{2.45}$$

Defining $F_n(\beta_d a, \beta_d b)$ as

$$F_n(\beta_d a, \beta_d b) = \frac{J_n(\beta_d b) Y_n(\beta_d a) \ - \ J_n(\beta_d a) Y_n(\beta_d b)}{Y_n(\beta_d a)} \tag{2.46}$$

equation (2.45) becomes

$$j^{-n} J_n(\beta_o b) + a_n H_n^{(2)}(\beta_o b) = b_n F_n(\beta_d a, \beta_d b) \ . \tag{2.47}$$

There are two unknowns, but only one equation. Another equation is needed. The tangential magnetic fields are required to get another equation. Maxwell's equation from Faraday's law is used to get the tangential magnetic fields,

$$\mathbf{H} = -\frac{1}{j\omega\mu} \nabla \times \mathbf{E}_z = -\frac{1}{j\omega\mu} \left(\hat{\rho} \frac{1}{\rho} \frac{\partial E_z}{\partial \phi} - \hat{\phi} \frac{\partial E_z}{\partial \rho} \right) \ . \tag{2.48}$$

Only the $\hat{\phi}$ component is needed since it is the tangential component required for continuity. The resulting tangential magnetic fields for the incident, scattered, and

dielectric fields are

$$H_\phi^i = \frac{E_o\beta_o}{j\omega\mu_o}\sum_{n=-\infty}^{+\infty} j^{-n}J_n'(\beta_o\rho)e^{jn\phi} \tag{2.49}$$

$$H_\phi^s = \frac{E_o\beta_o}{j\omega\mu_o}\sum_{n=-\infty}^{+\infty} a_n H_n^{(2)'}(\beta_o\rho)e^{jn\phi} \tag{2.50}$$

$$H_\phi^d = \frac{E_o\beta_d}{j\omega\mu}\sum_{n=-\infty}^{+\infty} \left[b_n J_n'(\beta_d\rho) + c_n Y_n'(\beta_d\rho)\right] e^{jn\phi} \tag{2.51}$$

where μ_o is the permeability of free space and μ is the permeability of the dielectric. Applying boundary conditions and enforcing continuity at the the air/dielectric interface at $(\rho = b)$, the free-space tangential magnetic fields must equal the tangential magnetic field in the dielectric,

$$(H_\phi^i + H_\phi^s)|_{\rho=b} = H_\phi^d|_{\rho=b}\ . \tag{2.52}$$

Substituting for the tangential incident, scattered, and dielectric magnetic fields, equation (2.52) becomes

$$\frac{E_o\beta_o}{j\omega\mu_o}\sum_{n=-\infty}^{+\infty}\left[j^{-n}J_n'(\beta_o b) + a_n H_n^{(2)'}(\beta_o b)\right]e^{jn\phi} = \frac{E_o\beta_d}{j\omega\mu}\sum_{n=-\infty}^{+\infty}\left[b_n J_n'(\beta_d b) + c_n Y_n'(\beta_d b)\right]e^{jn\phi}\ . \tag{2.53}$$

After dividing both sides by $\frac{E_o\beta_o}{j\omega\mu_o}$ and applying the orthogonal operator, $\frac{1}{2\pi}\int_{-\pi}^{\pi} e^{-jm\phi}\{\cdots\}d\phi$, equation (2.53) becomes,

$$j^{-n}J_n'(\beta_o b) + a_n H_n^{(2)'}(\beta_o b) = \frac{\beta_d\mu_o}{\beta_o\mu}\left[b_n J_n'(\beta_d b) + c_n Y_n'(\beta_d b)\right]\ . \tag{2.54}$$

Using the definition, $\beta = \omega\sqrt{\varepsilon\mu}$, with $\varepsilon = \varepsilon_o\varepsilon_r$ and $\mu = \mu_o\mu_r$ and the solution for c_n from equation (2.41), equation (2.54) can be simplified further,

$$j^{-n}J_n'(\beta_o b) + a_n H_n^{(2)'}(\beta_o b) = b_n\sqrt{\frac{\epsilon_r}{\mu_r}}\left[\frac{J_n'(\beta_d b)Y_n(\beta_d a)\ -\ J_n(\beta_d a)Y_n'(\beta_d b)}{Y_n(\beta_d a)}\right]\ . \tag{2.55}$$

Defining $G_n(\beta_d a, \beta_d b)$ as

$$G_n(\beta_d a, \beta_d b) = \frac{J_n'(\beta_d b)Y_n(\beta_d a) \; - \; J_n(\beta_d a)Y_n'(\beta_d b)}{Y_n(\beta_d a)} \tag{2.56}$$

equation (2.55) becomes

$$j^{-n}J_n'(\beta_o b) + a_n H_n^{(2)'}(\beta_o b) = b_n \sqrt{\frac{\varepsilon_r}{\mu_r}} G_n(\beta_d a, \beta_d b) \; . \tag{2.57}$$

Rewriting equations (2.47) and (2.57), there are two equations with two unknowns,

$$a_n H_n^{(2)}(\beta_o b) - b_n F_n(\beta_d a, \beta_d b) = -j^{-n}J_n(\beta_o b) \tag{2.58}$$

$$a_n H_n^{(2)'}(\beta_o b) - b_n \sqrt{\frac{\varepsilon_r}{\mu_r}} G_n(\beta_d a, \beta_d b) = -j^{-n}J_n'(\beta_o b) \; . \tag{2.59}$$

Multiplying equation (2.58) by $\sqrt{\frac{\varepsilon_r}{\mu_r}} G_n(\beta_d a, \beta_d b)$ and equation (2.59) by $F_n(\beta_d a, \beta_d b)$, subtracting equation (2.59) from equation (2.58), and solving for a_n gives

$$a_n = j^{-n} \frac{J_n'(\beta_o b)F_n(\beta_d a, \beta_d b) - \sqrt{\frac{\varepsilon_r}{\mu_r}} J_n(\beta_o b)G_n(\beta_d a, \beta_d b)}{\sqrt{\frac{\varepsilon_r}{\mu_r}} H_n^{(2)}(\beta_o b)G_n(\beta_d a, \beta_d b) - H_n^{(2)'}(\beta_o b)F_n(\beta_d a, \beta_d b)} \; . \tag{2.60}$$

Since only a_n is needed to calculate the far-field 2D RCS, b_n is not solved. Substituting the solution for a_n into equation (2.37) gives the magnitude field ratio for a 2D dielectric-coated PEC circular cylinder,

$$\frac{|\mathbf{E}^s|}{|\mathbf{E}^i|} \overset{\beta_o \rho \to large}{\cong} \sqrt{\frac{2}{\pi \beta_o \rho}} \left| \sum_{n=-\infty}^{+\infty} \frac{J_n'(\beta_o b)F_n(\beta_d a, \beta_d b) - \sqrt{\frac{\varepsilon_r}{\mu_r}} J_n(\beta_o b)G_n(\beta_d a, \beta_d b)}{\sqrt{\frac{\varepsilon_r}{\mu_r}} H_n^{(2)}(\beta_o b)G_n(\beta_d a, \beta_d b) - H_n^{(2)'}(\beta_o b)F_n(\beta_d a, \beta_d b)} e^{jn\phi} \right| \; . \tag{2.61}$$

The far-field TM^z 2D RCS for a dielectric-coated PEC circular cylinder is found using this ratio in equation (2.4). The next case to consider is the TE^z case.

2.4.2 TE^z Case. For the TE^z case, the incident magnetic field consists only of a $\hat{z}$ component. The TE^z case uses the incident and scattered magnetic fields,

$$\mathbf{H}^i = \hat{z}H_z^i = \hat{z}H_o e^{-j\beta_o x} = \hat{z}H_o \sum_{n=-\infty}^{+\infty} j^{-n} J_n(\beta_o \rho) e^{jn\phi} \tag{2.62}$$

$$\mathbf{H}^s = \hat{z}H_z^s = \hat{z}H_o \sum_{n=-\infty}^{+\infty} d_n H_n^{(2)}(\beta_o \rho) e^{jn\phi} \ , \tag{2.63}$$

in the scattering model. The variable d_n is the amplitude coefficient analogous to a_n from the previous section. The magnitude field ratio used for the TE^z 2D RCS is

$$\frac{|\mathbf{H}^s|}{|\mathbf{H}^i|} = \frac{\left| H_o \sum_{n=-\infty}^{+\infty} d_n H_n^{(2)}(\beta_o \rho) e^{jn\phi} \right|}{|H_o e^{-j\beta_o x}|} \ . \tag{2.64}$$

As before, the large argument approximation for the Hankel function is used for the far-field RCS. Substituting equation (2.30) for the Hankel function, equation (2.64) becomes

$$\frac{|\mathbf{H}^s|}{|\mathbf{H}^i|} \overset{\beta_o \rho \to large}{\cong} \sqrt{\frac{2}{\pi \beta_o \rho}} \left| \sum_{n=-\infty}^{+\infty} j^{-n} d_n e^{jn\phi} \right| \ . \tag{2.65}$$

The next step is to determine what d_n is for a PEC circular cylinder and a dielectric-coated PEC circular cylinder.

2.4.2.1 TE^z PEC Circular Cylinder. From Figure 2.9, there are two regions illustrated. Region I is free-space outside the PEC cylinder ($\rho > a$). Region II is the PEC region ($\rho < a$). The total field of region I is the sum of the incident field and scattered field. Since region II is a PEC, no fields exist in the region. Maxwell's equation from Ampere's law is used to get the tangential electric fields from the magnetic fields,

$$\mathbf{E} = \frac{1}{j\omega\varepsilon} \nabla \times \mathbf{H}_z = \frac{1}{j\omega\varepsilon} \left(\hat{\rho} \frac{1}{\rho} \frac{\partial H_z}{\partial \phi} - \hat{\phi} \frac{\partial H_z}{\partial \rho} \right) \ . \tag{2.66}$$

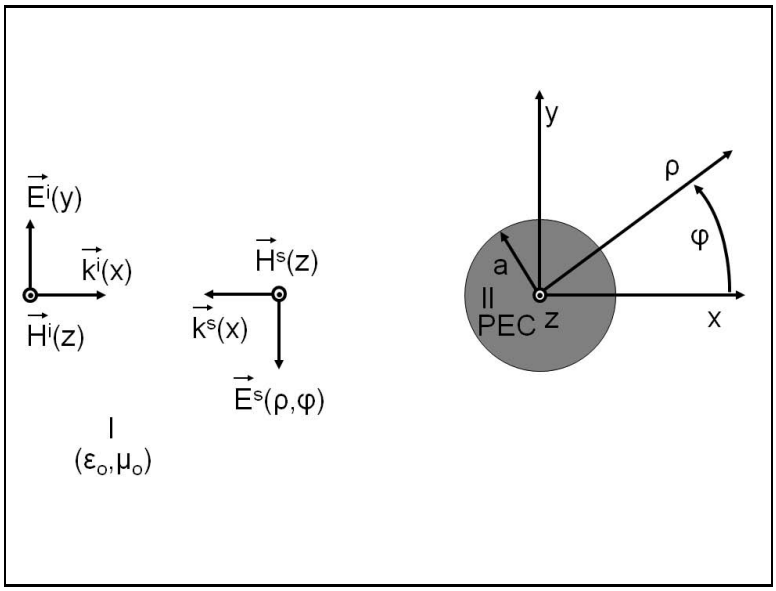

Figure 2.9: 2D PEC cylinder with TE^z illumination.

Only the $\hat{\phi}$ component is needed since it is the tangential component required for continuity. The tangential incident and scattered electric fields are

$$E_\phi^i = -\frac{H_o\beta_o}{j\omega\varepsilon_o}\sum_{n=-\infty}^{+\infty} j^{-n}J_n'(\beta_o\rho)e^{jn\phi} \tag{2.67}$$

$$E_\phi^s = -\frac{H_o\beta_o}{j\omega\varepsilon_o}\sum_{n=-\infty}^{+\infty} d_n H_n^{(2)'}(\beta_o\rho)e^{jn\phi} \tag{2.68}$$

where ε_o is the free-space permittivity. Since the boundary condition for a PEC states the tangential electric field PEC be zero, the tangential components of the total electric field at the surface must be zero,

$$E_\phi^t(\rho=a, 0\le\phi\le 2\pi, z) = -\frac{H_o\beta_o}{j\omega\epsilon_o}\sum_{n=-\infty}^{+\infty}\left[j^{-n}J_n'(\beta_o a) + d_n H_n^{(2)'}(\beta_o a)\right]e^{jn\phi} = 0\ . \tag{2.69}$$

In the same manner used to find a_n in Section 2.4.1.1, d_n is

$$d_n = -j^{-n}\frac{J_n'(\beta_o a)}{H_n^{(2)'}(\beta_o a)}\ . \tag{2.70}$$

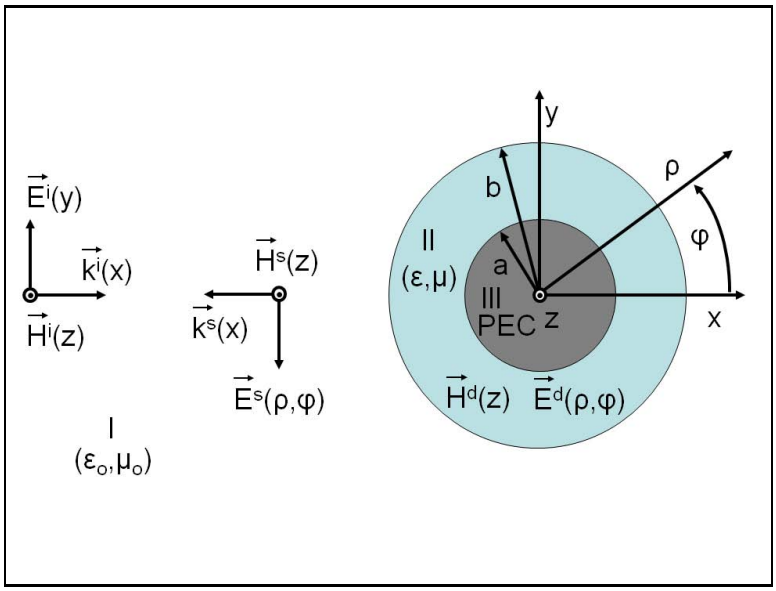

Figure 2.10: 2D dielectric-coated cylinder with TE^z illumination.

The magnitude field ratio for equation (2.4) is

$$\frac{|\mathbf{H}^s|}{|\mathbf{H}^i|} \overset{\beta_o\rho\rightarrow large}{\cong} \sqrt{\frac{2}{\pi\beta_o\rho}} \left| \sum_{n=-\infty}^{+\infty} \frac{J_n'(\beta_o a)}{H_n^{(2)'}(\beta_o a)} e^{jn\phi} \right| . \tag{2.71}$$

The final analytic model is the the TE^z dielectric-coated PEC circular cylinder case.

2.4.2.2 TE^z Dielectric-Coated PEC Circular Cylinder. The TE^z case for a dielectric-coated circular cylinder is considered in problem 11-28 in Balanis' text and solved in the solution manual [5]. The solution manual provides the foundation for the dielectric-coated circular cylinder analytic model. Figure 2.10 illustrates the dielectric region. Region I is the free-space region surrounding the target ($\rho > b$). Region II is the dielectric region ($a < \rho < b$), and region III is the PEC region ($\rho < a$). The fields in region I are the same as the previous section defined by equations (2.62) and (2.63). The total magnetic field in region II is the dielectric magnetic field ($\mathbf{H}^d$). As stated before, the field inside the PEC is zero. The magnetic field in the dielectric

is

$$\mathbf{H}^d = \hat{z} H_z^d = \hat{z} H_o \sum_{n=-\infty}^{+\infty} \left[g_n J_n(\beta_d \rho) + h_n Y_n(\beta_d \rho) \right] e^{jn\phi} \ . \tag{2.72}$$

Enforcing continuity at the boundaries, the tangential electric fields are required. The tangential incident and scattered electric fields are known from the previous section, all that is needed is the tangential dielectric electric field. It is found using equation (2.66) to be

$$E_\phi^d = -\frac{H_o \beta_d}{j\omega\varepsilon} \sum_{n=-\infty}^{+\infty} \left[g_n J_n'(\beta_d \rho) + h_n Y_n'(\beta_d \rho) \right] e^{jn\phi} \tag{2.73}$$

where ε is the permittivity of the dielectric material. To determine d_n, g_n, and h_n, the continuity conditions to satisfy are

$$E_\phi^d|_{\rho=a} = 0 \tag{2.74}$$

$$(E_\phi^i + E_\phi^s)|_{\rho=b} = E_\phi^d|_{\rho=b} \tag{2.75}$$

$$(H_z^i + H_z^s)|_{\rho=b} = H_z^d|_{\rho=b} \ . \tag{2.76}$$

Solving for d_n in the same manner to find a_n in Section 2.4.1.2 begets

$$d_n = j^{-n} \frac{J_n'(\beta_o b) F_n'(\beta_d a, \beta_d b) - \sqrt{\frac{\mu_r}{\varepsilon_r}} J_n(\beta_o b) G_n'(\beta_d a, \beta_d b)}{\sqrt{\frac{\mu_r}{\varepsilon_r}} H_n^{(2)}(\beta_o b) G_n'(\beta_d a, \beta_d b) - H_n^{(2)'}(\beta_o b) F_n'(\beta_d a, \beta_d b)} \tag{2.77}$$

where $F_n'(\beta_d a, \beta_d b)$ is

$$F_n'(\beta_d a, \beta_d b) = \frac{J_n(\beta_d b) J_n'(\beta_d a) \ - \ Y_n'(\beta_d a) Y_n(\beta_d b)}{J_n'(\beta_d a)} \tag{2.78}$$

and $G_n'(\beta_d a, \beta_d b)$ is

$$G_n'(\beta_d a, \beta_d b) = \frac{J_n'(\beta_d b) J_n'(\beta_d a) \ - \ Y_n'(\beta_d a) Y_n'(\beta_d b)}{J_n'(\beta_d a)} \ . \tag{2.79}$$

The magnitude field ratio for equation (2.4) is

$$\frac{|\mathbf{H}^s|}{|\mathbf{H}^i|} \overset{\beta_o\rho\to large}{\cong} \sqrt{\frac{2}{\pi\beta_o\rho}} \left| \sum_{n=-\infty}^{+\infty} \frac{J_n'(\beta_o b)F_n'(\beta_d a,\beta_d b) - \sqrt{\frac{\mu_r}{\varepsilon_r}} J_n(\beta_o b)G_n'(\beta_d a,\beta_d b)}{\sqrt{\frac{\mu_r}{\varepsilon_r}} H_n^{(2)}(\beta_o b)G_n'(\beta_d a,\beta_d b) - H_n^{(2)'}(\beta_o b)F_n'(\beta_d a,\beta_d b)} e^{jn\phi} \right| . \tag{2.80}$$

These analytic models are exact solutions to the scattering scenario. Computational EM software packages use numerical models in scattering analysis. One such application is the COMSOL Multiphysics suite.

2.5 Numeric Model

The previous section describes the exact solution to the scattering problem. Exact solutions become harder to formulate and solve as the problem becomes more complicated. For this reason, numerical models are introduced. Numerical models provide approximate solutions to the problem [14]. There are numerous computational electromagnetic software packages available. COMSOL Multiphysics software suite is used for this thesis. COMSOL uses the finite element method (FEM) to solve engineering problems. FEM techniques require the target and surrounding region to be discretized into a finite number of elements [11]. This is referred to as meshing. An example of meshing is shown in Figure 3.18. Using COMSOL, or any other comparable program, provides flexible analysis of models. Most commercial packages provide visualization tools enabling the user to better understand the solution.

III. Analysis Process

In order to characterize the scattering effect of the data-linked support string samples, a 2D RCS analysis approach is used. In addition to measuring the 2D RCS, an effort is made to model the complex structure of the strings as a single wire with a dielectric coating. This simple 2D model assumes the wire is a PEC and the dielectric is a linear, homogeneous, isotropic, and non-dispersive medium. Figure 3.1 illustrates the goals of this study. To accomplish these goals, there are seven steps in the process:

1. Measure the data-linked string 2D RCS with GTRI focus beam system
2. Generate reference target exact data for amplitude correction with Matlab®
3. Correct the measured data to obtain 2D RCS using Matlab®
4. Implement analytic model of dielectric-coated wire in Matlab®
5. Extract constitutive parameters by error minimization using Matlab®
6. Build simple 2D model in COMSOL and simulate 2D RCS
7. Compare COMSOL results with measured 2D RCS

The following sections detail these steps beginning with a description of the data-linked string samples.

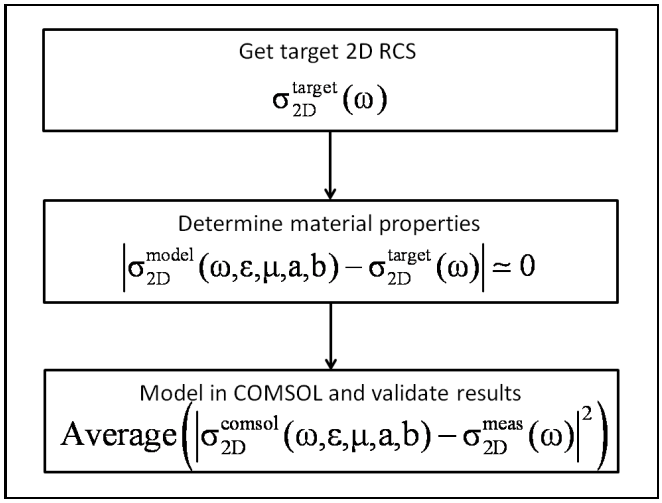

Figure 3.1: Goals of this thesis.

3.1 Target Description

Before detailing the measurement process, a description of the samples is in order. A total of four data-linked string samples are available for analysis. In addition to the string samples, two examples of ordinary insulated wire, 16 AWG and 12 AWG multi-strand wires (AWG stands for American wire gauge), are measured. The purpose of these targets is to validate the model of a dielectric-coated wire since, in fact, they are dielectric-coated wires. The data-linked support string samples vary in construction. All samples consist of a strength member required for its primary purpose, supporting structures. The strength member is a woven material similar to nylon string. The material of the strength member is unknown. Running through the center of the strength member are the data-link and conductors for power. Each sample contains copper wires. Each wire is insulated albeit the thickness is negligible. In addition to the copper wires, some samples contain a fiber optic cable. Table 3.1 describes the composition of each sample, referred to as targets. The targets are

Table 3.1: Target Description

Target	Wires	FO	Wire Diameter	Overall Diameter
Target 1	2	1	0.4 mm	$\simeq$ 1.65 mm
Target 2	2	0	0.25 mm	$\simeq$ 1.1 mm
Target 3	3	0	0.25 mm	$\simeq$ 1.7 mm
Target 4	5	1	0.4 mm	$\simeq$ 1.6 mm
Target 5	16 AWG	N/A	1.45 mm	2.9 mm
Target 6	12 AWG	N/A	2.4 mm	4.65 mm

shown in Figure 3.2. The difference in the strength members and string contents can be seen. Targets 5 and 6 are representative of the simple model approach to simplify the data-linked support strings.

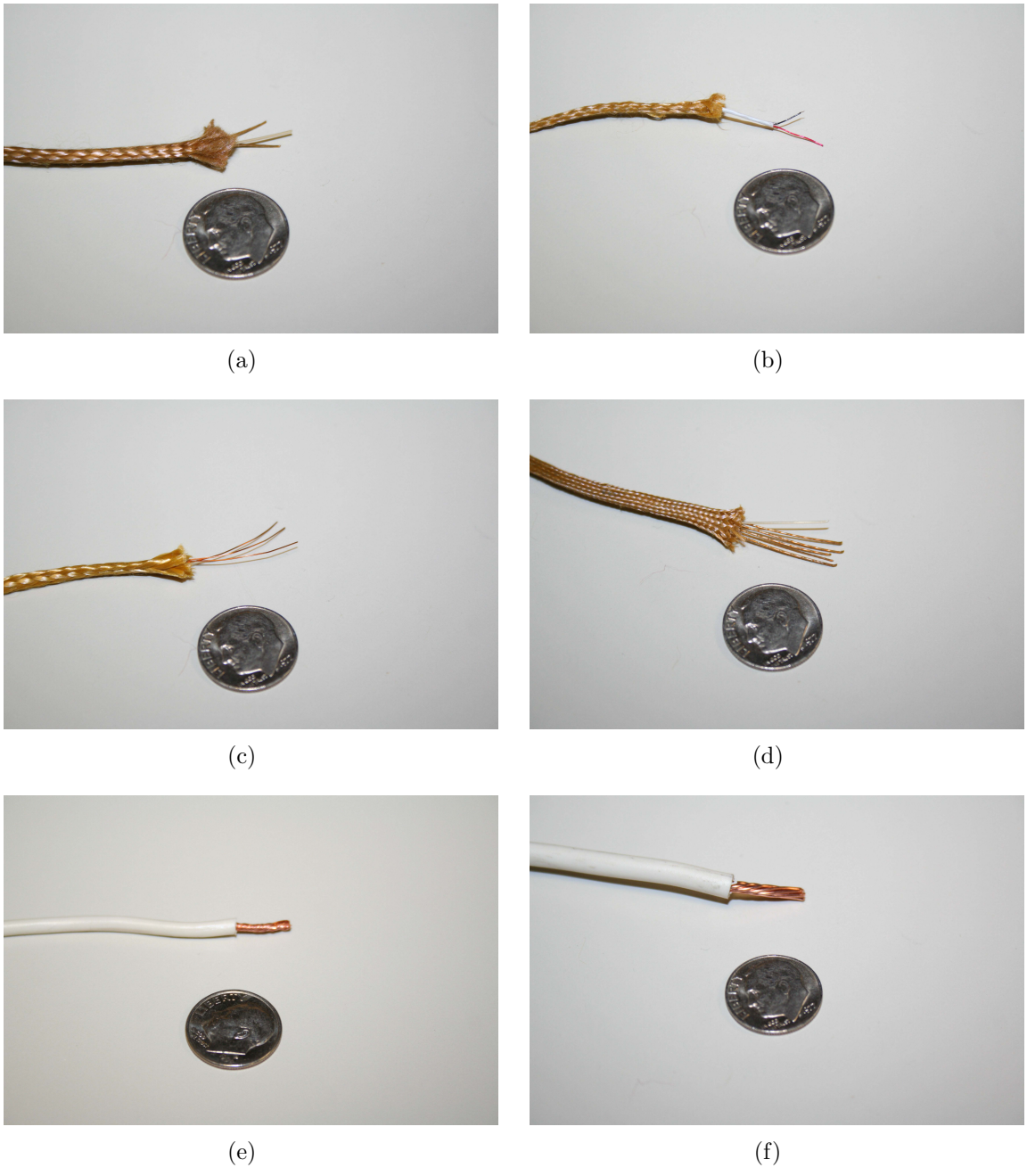

(a) (b)

(c) (d)

(e) (f)

Figure 3.2: (a) Data-linked string target 1, (b) data-linked string target 2, (c) data-linked string target 3, (d) data-linked string target 4, (e) dielectric-coated wire target 5, and (f) dielectric-coated wire target 6.

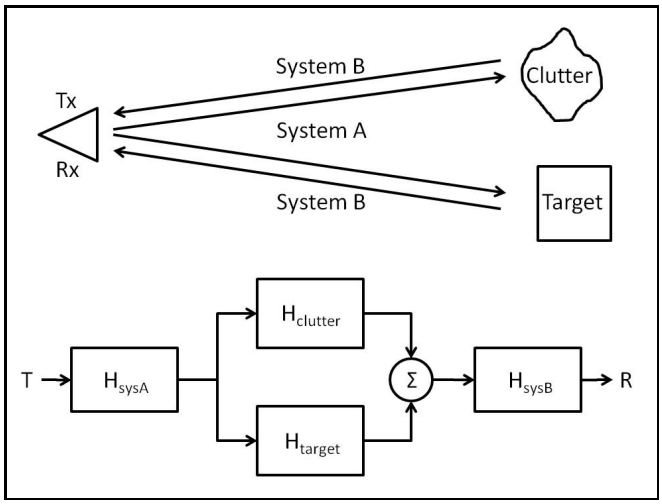

Figure 3.3: A system representation of the S-parameter measurement.

3.2 Scattering Parameters

Now that the targets for analysis are defined, the next step is to measure their scattering parameters, S-parameters, for both the TM^z and TE^z cases. The S-parameter data is complex valued and used to compute the 2D RCS. A systems approach is used to represent the measurement process. Figure 3.3 illustrates a very simplified model. The purpose of this discussion is to provide a basic understanding of what actually is measured when a measurement is taken. An antenna is used to launch or transmit, T_x, an EM wave of a specific frequency. The transmitted wave propagates to a scene containing a target. The medium of propagation from the antenna to this scene is considered system A. The transmitted wave scatters when it interacts with the target as well as anything else in the scene. The resulting scatter from anything but the target is considered clutter scattering. There is interaction between different components of the clutter, interaction between the target and clutter, and interaction between the target and its support. The antenna receives, R_x, the energy scattered in its direction. System B is considered the medium between the scatterers and the receiving antenna. This particular configuration represents a monostatic scattering analysis because the T_x and R_x antennas are the same antenna.

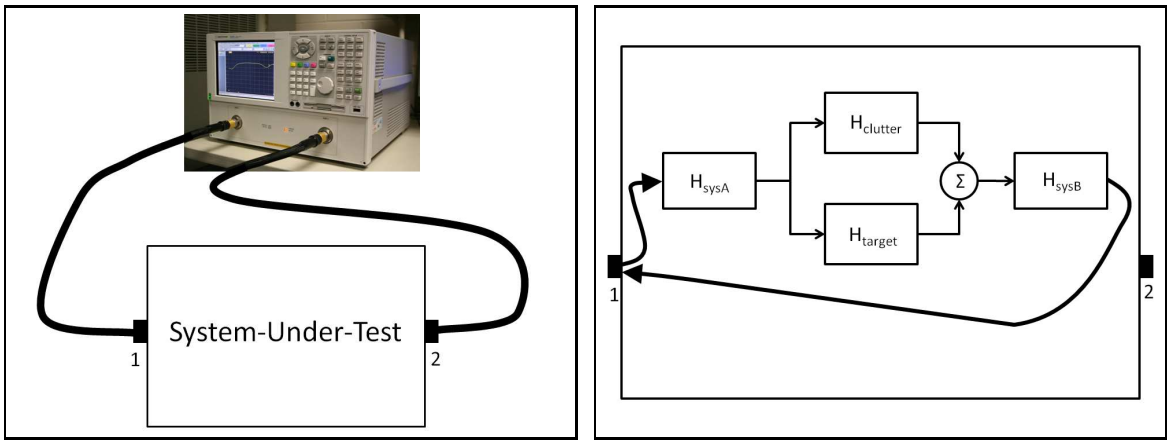

(a) (b)

Figure 3.4: (a) The PNA as a 2-port system analyzer and (b) monostatic RCS measurement system.

This approach works for a bistatic configuration as well. In the frequency domain where the measurements are obtained, the frequency response, H, of each component is used and illustrated at the bottom of Figure 3.3. The analysis is simplified because the resulting interaction between the transmitted wave and system components is the multiplication of the two. The entire system response is

$$R_x = (H_{sysA}H_{sysB}H_{target})T_x + (H_{sysA}H_{sysB}H_{clutter})T_x \tag{3.1}$$

where sysA is system A and sysB is system B. The S-parameter data is a function of the system response. It is the ratio of the received signal to the transmitted signal,

$$S_{out,in} = \frac{R_x}{T_x} = (H_{sysA}H_{sysB}H_{target}) + (H_{sysA}H_{sysB}H_{clutter}) \tag{3.2}$$

where the subscripts of S designates the input and output ports of the system.

The Agilent E8362B parametric network analyzer (PNA) is a 2-port system analyzer capable of measuring S-parameters data. Figure 3.4 (a) shows the PNA as a 2-port system analyzer. Consider the PNA analyzing the S-parameter data of the monostatic system described earlier. Figure 3.4 (b) shows port one is both the input

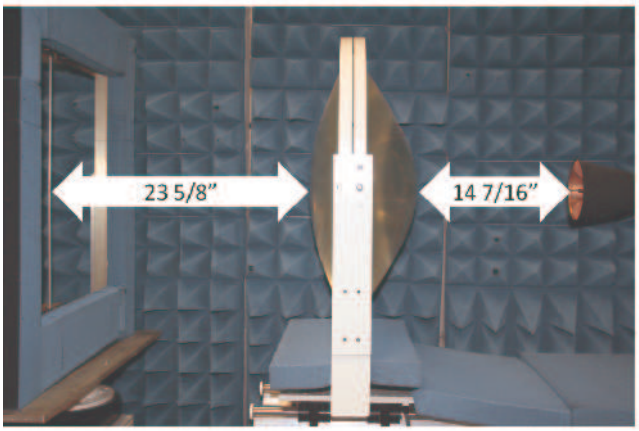

Figure 3.5: GTRI focus beam set-up and alignment.

(T_x) and output (R_x) port. This represents the monostatic S-parameter measurement of a target and is referred to as S_{11} data.

3.3 Target Measurement

3.3.1 Focus Beam Set-up. The PNA is used to obtain the S_{11} data of a system. The overall system-under-test is the GTRI focus beam system with the target mounted in the mounting frame. The port of the system is the input to the antenna. A side view of the system set-up is seen in Figure 3.5. The lens and antenna are positioned in accordance with the user manual [1] to achieve a focused planar wave at the target location. The resulting S-parameter data contains data from both the target and clutter. Clutter data is undesired because it contaminates the true S-parameter data of the target. In an effort to reduce the effects of clutter, RAM panels are placed around the focus beam to absorb and attenuate spurious illuminations. Figure 3.6 (a) shows the RAM placement around the target frame, and Figure 3.6 (b) shows how the target is mounted on frame. In addition to the panels, RAM is attached to the front face of the frame to reduce its clutter contribution. Recall the focus beam amplitude profile at the target is a Gaussian profile. Even though the illumination

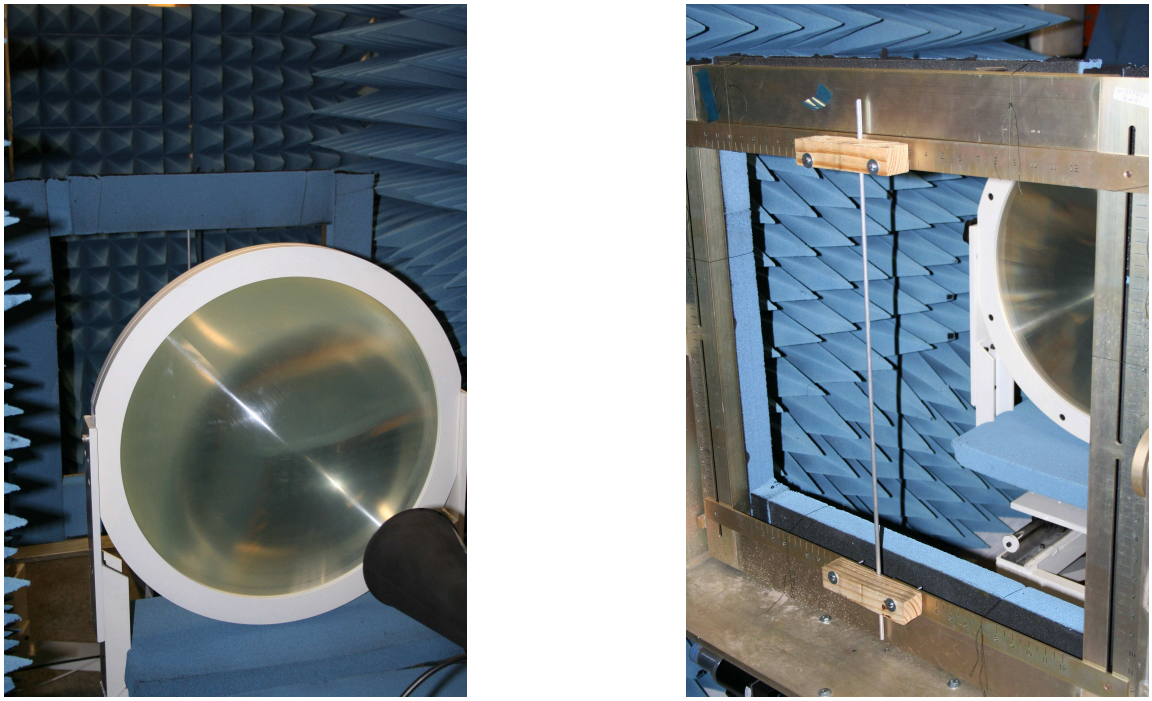

(a) (b)

Figure 3.6: (a) Down range view of focus beam showing RAM placement to reduce clutter and (b) a view of target mounted on frame.

area is considered within the beamwaist (where the amplitude of the beam is reduced by $1/e$) of the focused beam, the incident field amplitude is not zero outside of the beamwaist. For low frequencies with larger beamwaists, this is a concern. Figure 3.7 shows the normalized Gaussian amplitude profile for the frequency limits of the measurements overlaid on the target frame without RAM applied. The scattering from the frame is not as much of a concern for the 18 GHz case. However for the 2 GHz case, there is still sufficient amplitude outside of the beamwaist to cause concern and warrant adding RAM to the frame.

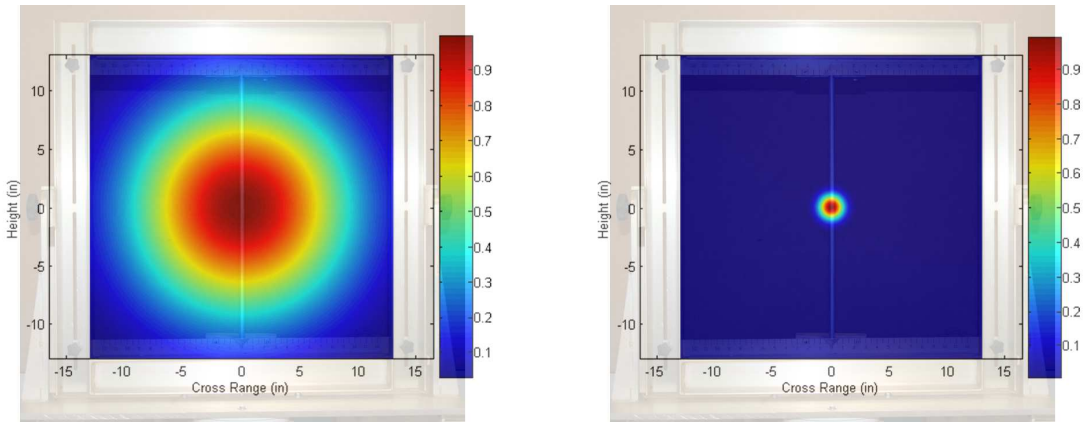

(a) (b)

Figure 3.7: (a) The normalized Gaussian amplitude profile at 2 GHz with respect to the mounting frame and (b) the normalized Gaussian amplitude profile at 18 GHz.

Both TM^z and TE^z S_{11} data is obtained without repositioning the target or rotating the antenna because the antenna has two feed ports, one for each polarization. A manual switch is used to select the polarization of the measurement. Figure 3.8 shows the antenna with the switch routing the input signal to either port.

Figure 3.8: Two ports for orthogonal polarization connected to routing switch.

After the focus beam system is set-up to take measurements, the next step is to set-up the PNA.

3.3.2 PNA Set-up. The PNA generates continuous wave (CW) RF energy. The generated RF is connected to the antenna to be transmitted. In addition to generating the RF, the PNA measures the reflected RF received by the antenna. The PNA divides the received signal by the the transmitted signal to obtain the S_{11} data (reference equation (3.2)). Table 3.2 shows the PNA settings for the scattering analysis. The frequency step size, δf, is 40 MHz with this number of points/sweep.

Table 3.2: PNA Settings

Frequency range	2-18 GHz
Frequency sweep type	Linear
Number of points/sweep	401
Power level	0 dBm
IFBW	1 kHz
Averaging	10

Receivers have internal noise either from heat or from RF components. Noise reduces the dynamic range of a receiver making its ability to detect low power signals difficult. The PNA has two noise reducing techniques. One method is averaging successive sweeps. Since thermal noise has a zero mean, its undesired effects can be reduced with averaging. Averaging improves the signal-to-noise ratio. As the number of sweeps averaged is increased, averaging can become a slow process. Another method to improve the signal-to-noise ratio is narrowing the intermediate frequency bandwidth (IFBW) of the PNA. This reduces the noise bandwidth effectively reducing the noise power. However, the narrower the IFBW, more steps are required to span the entire frequency range of 2-18 GHz for each measurement.

Another powerful method to ensure quality data acquisition is to gate the received RF in time. This cleans the response by ignoring the received RF before and after the gate window. To set the gate start and stop times, the location of the target plane is determined by observing the time domain response of an empty scene in con-

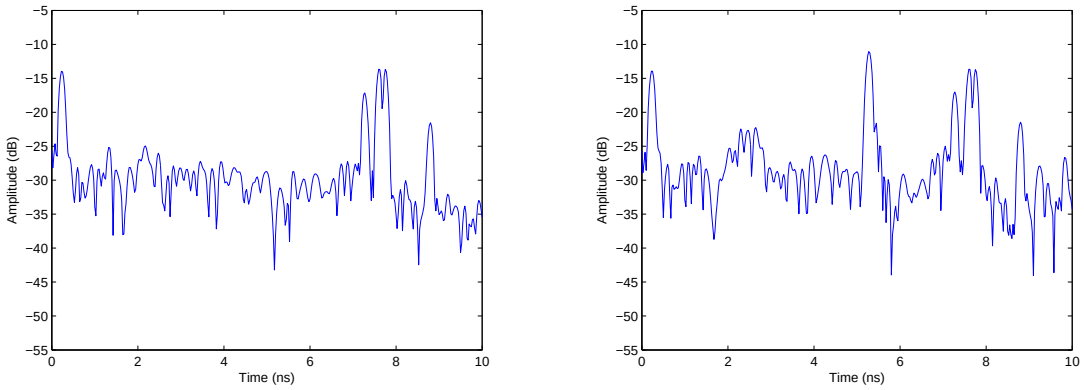

(a) (b)

Figure 3.9: (a) Time domain reflection measurement of empty scene and (b) time domain reflection measurement with flat plate at target location.

trast to a flat plate mounted in the target frame. Figure 3.9 shows the resulting time domain plots. The target plane, x_o, location in time is determined by the maximum amplitude of the plate reflection. From this reference point in time, the gate is set to $x_o \pm 3$ in by starting it 0.254 ns before and after the peak of the flat plate response. The choice of 3 in is small enough to mitigate multi-bounce reflections between the target and the mount and large enough to adequately capture the time extent of the target. The effects of gating are seen in Figure 3.10. The frequency response of the flat plate becomes stable over the frequency range. When the PNA is set-up and connected to the GTRI focus beam system, the system is ready to measure the S_{11} parameters of the targets.

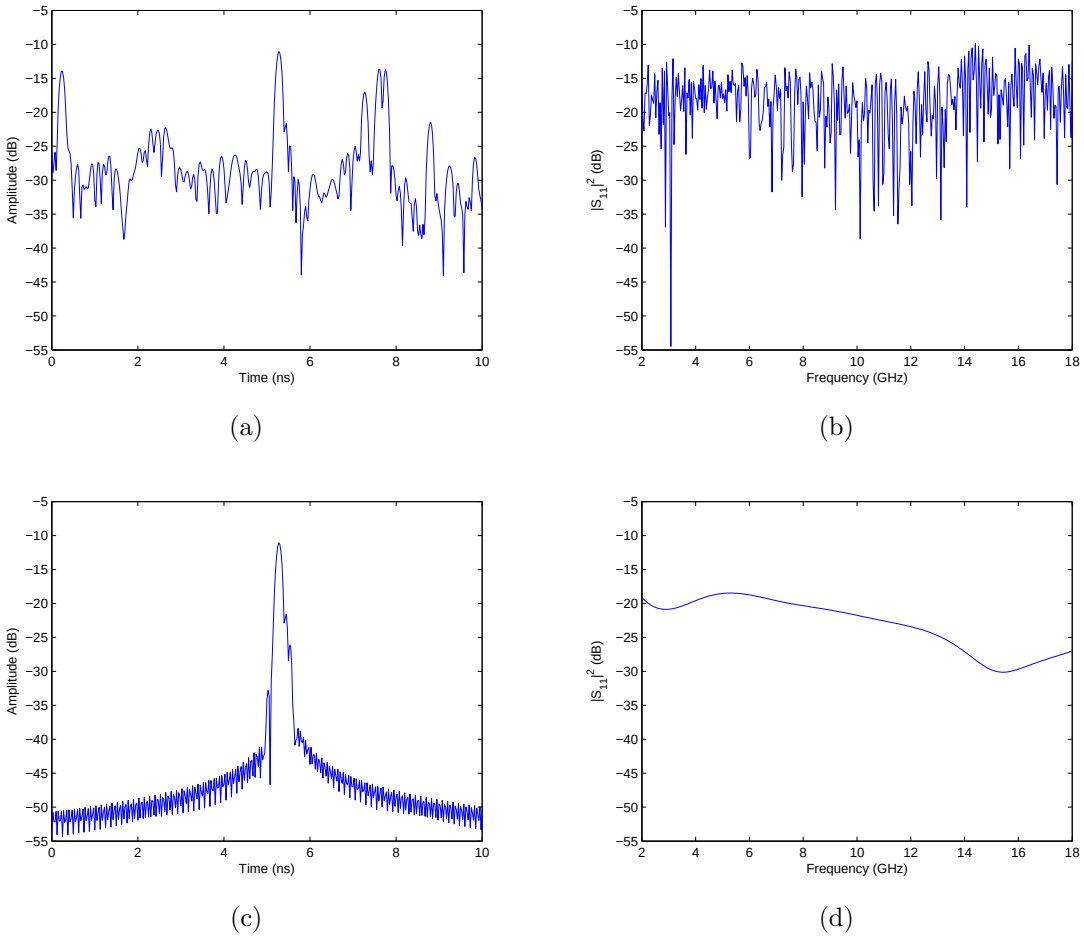

Figure 3.10: (a) Time domain reflection with flat plate at target location, (b) frequency domain response of flat plate, (c) gated time domain reflection of flat plate, and (d) frequency domain response of flat plate with gate applied.

3.3.3 S_{11} Measurement. The targets are placed vertically in the frame with wooden clamps. Special attention is given to ensure the target is centered in the frame and plumb for normal incident illumination. This is the assumption for 2D scattering analysis. The targets are stretched taut to remove slack in the strength member and the internal wires. When a target is set, the PNA averaging is started. The target is frequency swept 10 times and the results are averaged. After averaging, the S_{11} data is saved as a ".s1p" file. Saving the data in this format ensures PNA calibration factors are not applied to the data before saving. For each test configuration, the

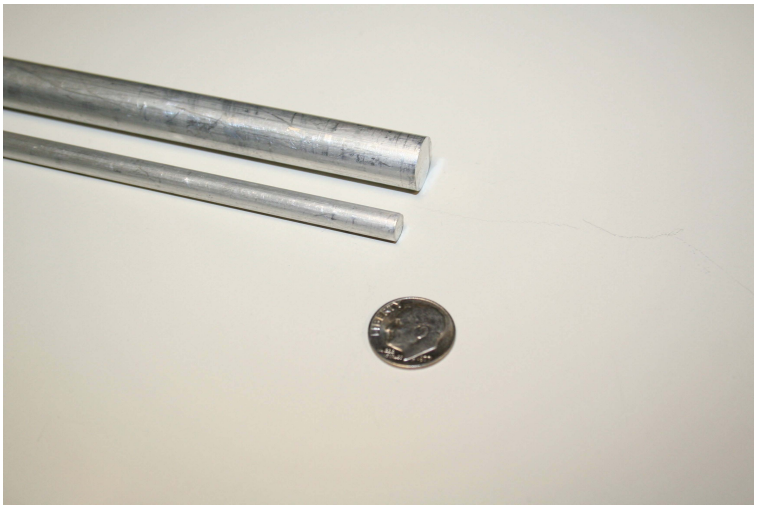

Figure 3.11: Two aluminum rods are used for the correction process. The radii are 1/4 in (6.35 mm) and 1/8 in (3.175 mm).

target is physically removed and replaced in the frame. The measurement is repeated five times in an attempt to quantify variability of the measurement set-up. In addition to the target measurements, a measurement of an empty scene is needed for coherent background subtraction. Background subtraction attempts to remove the clutter that remains inside the time gate. Two background measurements are taken. One at the beginning of the measurement session and one at the end. The two background measurements are compared to determine if the clutter scene changed during the entire process. Finally, two reference targets are measured. Figure 3.11 is a picture of the reference targets. A reference target is used to correct the amplitude of the S-parameter measurements and convert them to a 2D RCS.

3.4 Data Correction

The ".s1p" data from the PNA is imported into Matlab® for conversion to the 2D RCS. The conversion process performs two functions, coherent background subtraction and amplitude correction. Both are discussed in more detail in the following subsections.

3.4.1 Background Subtraction. The goal is to measure the S-parameter data of the targets. Unfortunately, Figure 3.3 shows clutter data is included in the measurement. Although steps were taken to reduce the clutter contribution, more is required to improve the accuracy of the measurement. Coherent background subtraction improves the accuracy by subtracting out the clutter, or background, contribution that remains in the time extent of the gate. The S_{11} data measured by the PNA is shown in equation (3.3),

$$S_{11}^{target} = (H_{sysA}H_{sysB})(H_{target} + H_{clutter}) \ . \tag{3.3}$$

Without a target present, equation (3.3) becomes the S_{11} data for the clutter,

$$S_{11}^{clutter} = (H_{sysA}H_{sysB})H_{clutter} \ . \tag{3.4}$$

Equation (3.5) shows coherent background subtraction is simply subtracting the S-parameter data of the clutter from the S-parameter data of the target,

$$S_{11}^{target} - S_{11}^{clutter} = (H_{sysA}H_{sysB})(H_{target} + H_{clutter}) - (H_{sysA}H_{sysB})H_{clutter} \ . \tag{3.5}$$

After simplifying, equation (3.6) shows the background subtracted data does not include the frequency response of the clutter,

$$S_{11}^{target} - S_{11}^{clutter} = (H_{sysA}H_{sysB})H_{target} \ . \tag{3.6}$$

Solving for H_{target} gives the frequency response of the target,

$$H_{target} = \frac{S_{11}^{target} - S_{11}^{clutter}}{H_{sysA}H_{sysB}} \ . \tag{3.7}$$

The frequency response of the target is not exact. There are amplitude errors in the data associated with the measurement system. To account for this error and correct it, the frequency response of the target needs to be amplitude corrected.

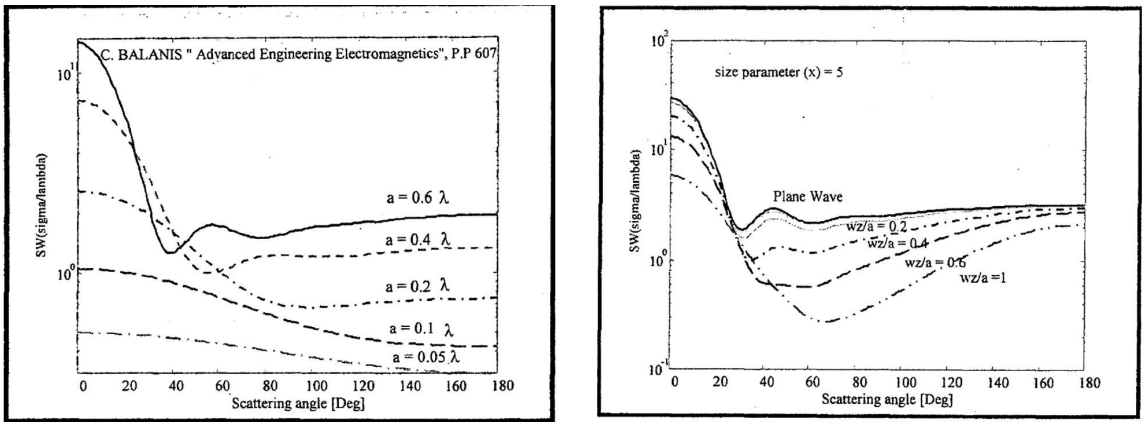

(a) (b)

Figure 3.12: (a) Reproduction of Balanis' plot of 2D RCS of PEC cylinder vs. bistatic angle for plane wave illumination [4] and (b) amplitude variation for PEC cylinder's 2D RCS vs. bistatic angle for Gaussian beam illumination [4].

3.4.2 Amplitude Correction. Gain of the antenna, attenuation in the lens, and the Gaussian amplitude profile of the focus beam are some sources of amplitude error. For instance, Figure 3.12 (b) shows how the magnitude of the TM^z 2D RCS of a cylinder differs for various beamwaist to cylinder radius ratios [4]. Amplitude correction involves measuring a reference target with a known solution for its frequency response. For instance, the exact solutions for canonical shapes such as PEC spheres and cylinders are known [5]. An aluminum rod is used as the reference target because its is representative of a PEC cylinder. For purposes of evaluating the correction process, a second reference target is required to compare its corrected 2D RCS with its exact 2D RCS values. Consider the target in equation (3.7) is the reference target,

$$H_{reference} = \frac{S_{11}^{reference} - S_{11}^{clutter}}{H_{sysA} H_{sysB}} \ . \tag{3.8}$$

Solving for $H_{sysA}H_{sysB}$ in equation (3.8) and substituting in (3.7) gives the frequency response of the target as a function of the ratio of the reference target's frequency

response and its S-parameter data,

$$H_{target} = (S_{11}^{target} - S_{11}^{clutter}) \left(\frac{H_{reference}}{S_{11}^{reference} - S_{11}^{clutter}} \right) \ . \tag{3.9}$$

The exact 2D RCS of the reference target can be calculated. Substituting the exact 2D RCS of the reference target in place of $H_{reference}$ and squaring the magnitudes of the measured S-parameter data of both the target and the reference target gives the amplitude corrected 2D RCS of the target,

$$\sigma_{2D}^{target} = \left| S_{11}^{target} - S_{11}^{clutter} \right|^2 \left(\frac{\sigma_{2D}^{reference}}{\left| S_{11}^{reference} - S_{11}^{clutter} \right|^2} \right) \ . \tag{3.10}$$

Equation (3.10) requires the exact 2D RCS for the reference target. The next step is to generate the exact data.

3.5 Exact Reference Data Generation

The 2D RCS solution is given in equation (2.4). The exact 2D RCS equation of a PEC cylinder with radius, a, is determined by substituting the solution for the ratio, $\frac{|\mathbf{E}^s|}{|\mathbf{E}^i|}$, from equation (2.37) for the TM^z case or equation (2.71) for the TE^z case,

$$\sigma_{2D_{PEC}}^{TM^z} = \lim_{\rho \to \infty} \left[2\pi\rho \frac{|\mathbf{E}^s|^2}{|\mathbf{E}^i|^2} \right] = \frac{4}{\beta_o} \left| \sum_{n=-\infty}^{+\infty} \frac{J_n(\beta_o a)}{H_n^{(2)}(\beta_o a)} e^{jn\phi} \right|^2 \tag{3.11}$$

$$\sigma_{2D_{PEC}}^{TE^z} = \lim_{\rho \to \infty} \left[2\pi\rho \frac{|\mathbf{E}^s|^2}{|\mathbf{E}^i|^2} \right] = \frac{4}{\beta_o} \left| \sum_{n=-\infty}^{+\infty} \frac{J_n'(\beta_o a)}{H_n^{(2)'}(\beta_o a)} e^{jn\phi} \right|^2 \ , \tag{3.12}$$

respectively.

To get the exact 2D RCS of the reference target, an analytic model is used. Equations (3.11) and (3.14) are implemented in Matlab®. The solution requires an infinite summation. However, the summation can be truncated to a finite summation from -N to N for an approximate solution. The degree of accuracy is dependent on the

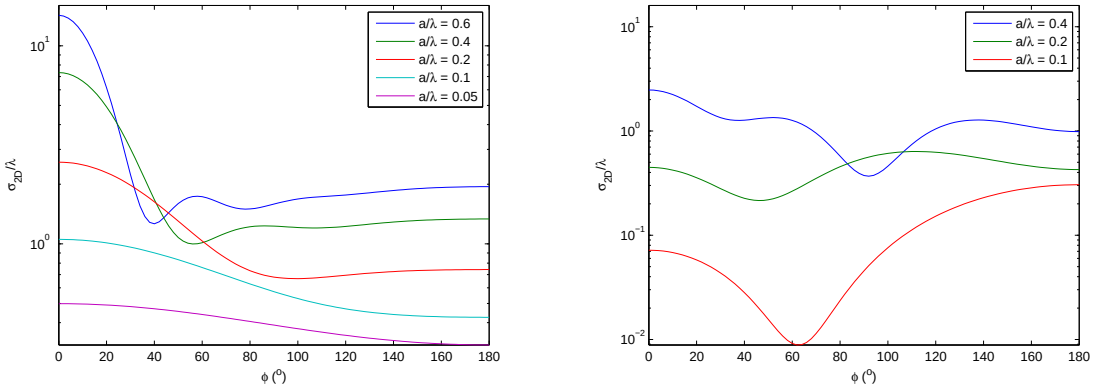

(a) (b)

Figure 3.13: (a) Analytic model reproduction of Figure 11-13 in Balanis [5] for TM^z case and (b) analytic model reproduction of Figure 11-15 in Balanis [5] for TE^z case.

number of terms in the summation. The number of terms necessary depends on the size of the argument in the Bessel and Hankel function. Fortunately, the argument in the Bessel and Hankel is relatively small for this case. The maximum argument is 2.394 for the 1/2-in reference target at 18 GHz. For this case, $N = 6$ is all that is required because the mean squared error between the solution for $N = 6$ and $N = 7$ is less than 10^{-6}.

Figure 3.13 is an exact reproduction of the reference figures published in Balanis [5] using the Matlab® function developed for this study effort. The analytic model is solved at the same frequencies used to measure the targets. Using the coordinate system defined in Figure 2.7, the angle ϕ for monostatic illumination is 180°. This is the same for the TE^z case. The radius of the reference target is used to generate the exact 2D RCS values needed to correct the amplitude of the 2D RCS of the targets. The exact data of the second aluminum rod is generated for comparison with its corrected measured 2D RCS as a correction process verification. The corrected 2D RCS can be used to determine the constitutive parameters of the simple dielectric-coated wire model.

3.6 Dielectric-Coated Wire Model Development

In the same manner as the previous section, the exact 2D RCS equation of a dielectric-coated cylinder is determined by substituting the solution for the ratio, $\frac{|\mathbf{E}^s|}{|\mathbf{E}^i|}$, from equation (2.61) for the TM^z case or equation (2.80) for the TE^z case into equation (2.4). The 2D RCS for a dielectric-coated wire model for the two cases become,

$$\sigma_{2D_{model}}^{TM^z} = \frac{4}{\beta_o}\left|\sum_{n=-\infty}^{+\infty}\frac{J_n'(\beta_o b)F_n(\beta_d a,\beta_d b) - \sqrt{\frac{\varepsilon_r}{\mu_r}}J_n(\beta_o b)G_n(\beta_d a,\beta_d b)}{\sqrt{\frac{\varepsilon_r}{\mu_r}}H_n^{(2)}(\beta_o b)G_n(\beta_d a,\beta_d b) - H_n^{(2)'}(\beta_o b)F_n(\beta_d a,\beta_d b)}e^{jn\phi}\right|^2 \tag{3.13}$$

$$\sigma_{2D_{model}}^{TE^z} = \frac{4}{\beta_o}\left|\sum_{n=-\infty}^{+\infty}\frac{J_n'(\beta_o b)F_n'(\beta_d a,\beta_d b) - \sqrt{\frac{\mu_r}{\varepsilon_r}}J_n(\beta_o b)G_n'(\beta_d a,\beta_d b)}{\sqrt{\frac{\mu_r}{\varepsilon_r}}H_n^{(2)}(\beta_o b)G_n'(\beta_d a,\beta_d b) - H_n^{(2)'}(\beta_o b)F_n'(\beta_d a,\beta_d b)}e^{jn\phi}\right|^2 \tag{3.14}$$

where $F_n(\beta_d a,\beta_d b)$, $G_n(\beta_d a,\beta_d b)$, $F_n'(\beta_d a,\beta_d b)$, and $G_n'(\beta_d a,\beta_d b)$ are defined in equations (2.46), (2.56), (2.78), and (2.79) respectively. The maximum radius to consider is the dielectric radius for target 6, 2.325 mm. Since the targets are smaller in radius than the reference targets, the limits of the summation are on the same order. As a precaution, $N = 15$ is used to ensure sufficient terms in the model. The solution of a dielectrically-coated cylinder with PEC radius, a, dielectric radius, b, and relative permittivity and relative permeability of 1 is considered as a special case where the dielectric is air. The results of this dielectric-coated model are compared to the results of the verified model in the previous section of a PEC with radius, a. They should be identical. However, implementing equation (3.13) in Matlab® results in diverging solutions as seen in Figure 3.14. Another approach to implementing the dielectric-coated wire model is to use matrix algebra.

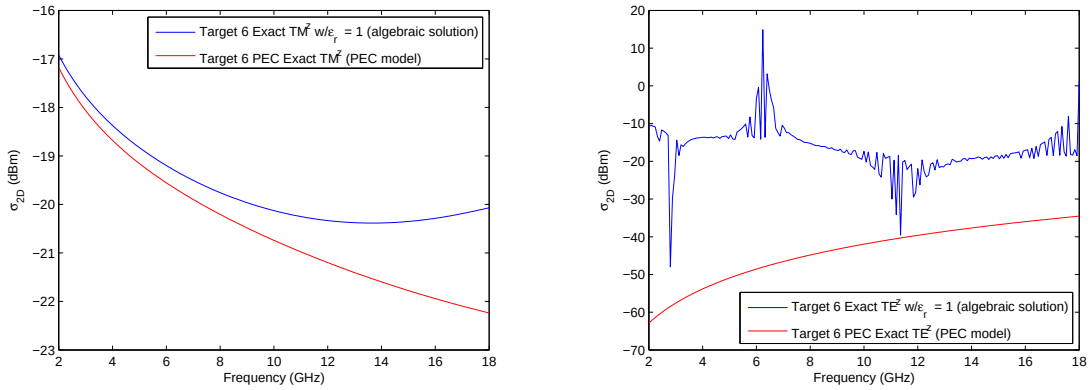

(a) (b)

Figure 3.14: (a) Error in analytic model results for TM^z case and (b) error in analytic model results for TE^z case.

The boundary conditions for both TM^z and TE^z orientation each provide a system of three linear equations with three unknowns. Matrix algebra provides another approach for implementing the model. For the TM^z case, the boundary conditions defined in equations (2.40), (2.44), and (2.54) can be re-arranged into a system of linear equations.

$$\begin{aligned} J_n(\beta_d a)b_n + Y_n(\beta_d a)c_n &= 0 \\ H_n^{(2)}(\beta_o b)a_n - J_n(\beta_d b)b_n - Y_n(\beta_d b)c_n &= -j^{-n}J_n(\beta_o b) \\ H_n^{(2)'}(\beta_o b)a_n - \sqrt{\frac{\varepsilon_r}{\mu_r}}J_n'(\beta_d b)b_n - \sqrt{\frac{\varepsilon_r}{\mu_r}}Y_n'(\beta_d b)c_n &= -j^{-n}J_n'(\beta_o b) \end{aligned}$$

Systems of linear equations may be decomposed into matrix and vector components [18] and solved using matrix algebra. The variables of the system are the amplitude coefficients, a_n, b_n, and c_n. They form the variable column vector, $\mathbf{x}$,

$$\mathbf{x} = \begin{bmatrix} a_n \\ b_n \\ c_n \end{bmatrix} \tag{3.15}$$

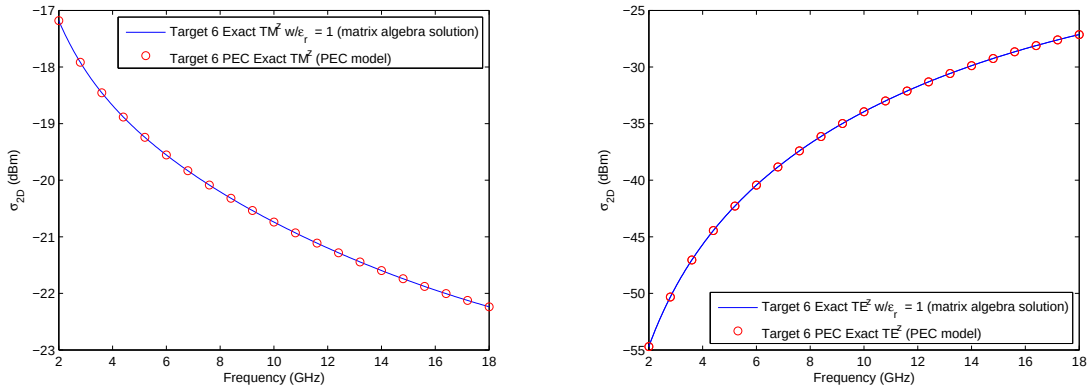

(a) (b)

Figure 3.15: (a) Dielectric-coated PEC analytic model verify for TM^z case and (b) Dielectric-coated PEC analytic model verify for TE^z case.

The coefficients of the variables are put into the coefficient matrix, A,

$$A = \begin{bmatrix} 0 & J_n(\beta_d a) & Y_n(\beta_d a) \\ H_n^{(2)}(\beta_o b) & -J_n(\beta_d b) & -Y_n(\beta_d b) \\ H_n^{(2)'}(\beta_o b) & -\sqrt{\frac{\varepsilon_r}{\mu_r}} J_n'(\beta_d b) & -\sqrt{\frac{\varepsilon_r}{\mu_r}} Y_n'(\beta_d b) \end{bmatrix} \tag{3.16}$$

Finally, the right-hand side of the equations form the column vector, $\mathbf{b}$,

$$\mathbf{b} = \begin{bmatrix} 0 \\ -j^{-n} J_n(\beta_o b) \\ -j^{-n} J_n'(\beta_o b) \end{bmatrix} \tag{3.17}$$

The only solution to $\mathbf{x}$ is $A^{-1}\mathbf{b}$ if A is invertible [18]. Using this approach in Matlab® for both the TE^z and TM^z case resolves the error seen in Figure 3.14 for the air dielectric case. The verification of the TE^z and TM^z dielectric-coated PEC analytic models is seen in Figure 3.15 and Figure 3.16.

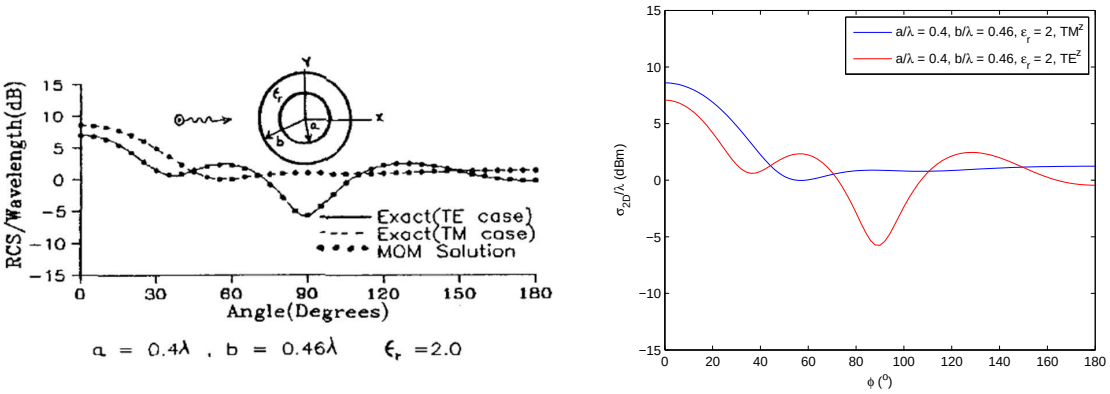

(a) (b)

Figure 3.16: (a) Dielectric-coated PEC exact solution results [20] and (b) analytic model for dielectric-coated PEC results.

In order to model the exact 2D RCS of a dielectric-coated wire, the analytic model requires the input of four variables:

1. radius of PEC wire, a
2. radius of the dielectric coating, b
3. relative permittivity of the dielectric coating, ε_r
4. relative permeability of the dielectric coating, μ_r

The values for variables 1 and 2 can be estimated from the physical construction of the targets. Using information from Table 3.1, an approximation is used to estimate the radius of the PEC for targets 1-4. The total PEC cross-sectional area is calculated by adding the cross-sectional areas of each wire contained in the target. The PEC radius used in the model is the radius of a circle with the equivalent area. This method for estimating the PEC radius is a better approximation for some of the samples than it is for others based on Figure 3.17. The dielectric radius used for a target is half the overall diameter of the target. For targets 1-4, the error in the estimation of both radii varies. For targets 5 and 6, this error is reduced by the consistency of their construction. As for the constitutive parameters, ε_r and μ_r, they are estimated using the measured data. The next section discusses the estimation procedure.

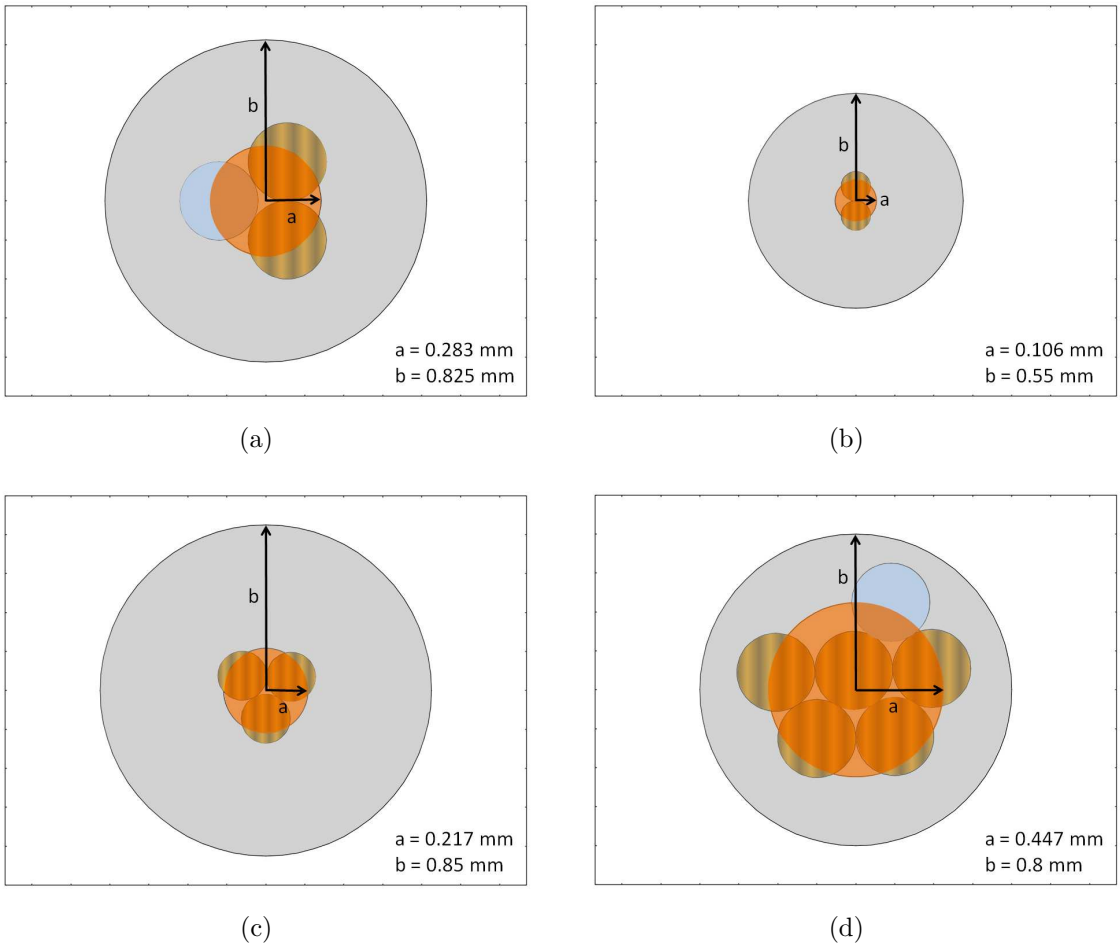

Figure 3.17: Estimated PEC and dielectric radii for (a) target 1, (b) target 2, (c) target 3, and (d) target 4.

3.7 Constitutive Parameters Estimation

The constitutive parameter estimation process is an iterative process of comparing the measured 2D RCS of the target with the simple dielectric-coated model 2D RCS. With the PEC radius and dielectric coating radius set, the model's 2D RCS becomes a function of ε_r and μ_r. Both ε_r and μ_r can be complex valued. However, two assumptions are made about the material properties which simplifies the parameter estimation process. The first assumption assumes the relative permeability is 1 for all of the targets. This assumption is reasonable because the string material does not

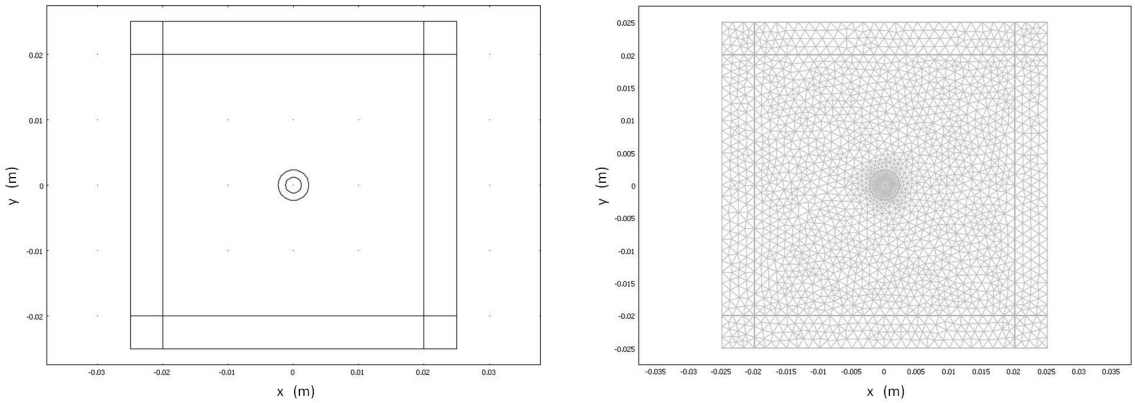

(a) (b)

Figure 3.18: (a) 2D geometry of target 6 and (b) the geometry meshed.

seem to have magnetic properties. Now the model's 2D RCS is a function of ε_r only. The second assumption assumes the dielectric constant is purely real valued.

Comparing the measured 2D RCS of a target to the dielectric-coated wire model at each frequency while adjusting the relative permittivity of the dielectric-coated wire model enables the estimation of the effective dielectric constant of the target. This is implemented in Matlab® by determining the relative permittivity that minimizes the error between the measured and modeled 2D RCS of each target. The values of the model are used to perform a numerical model analysis using COMSOL Multiphysics software.

3.8 Numerical Model Analysis

COMSOL is a convenient tool for 2D RCS analysis. Both TE^z and TM^z analysis can be performed. The purpose of this section is not to provide a step-by-step "how to" to use COMSOL. Instead, this section covers the general set-up of the model for TM^z and TE^z analysis. As stated in the previous chapter, FEM techniques require a defined region for analysis instead of just the target. Figure 3.18 shows the defined region to be analyzed and the required meshing for FEM techniques. The radius of the

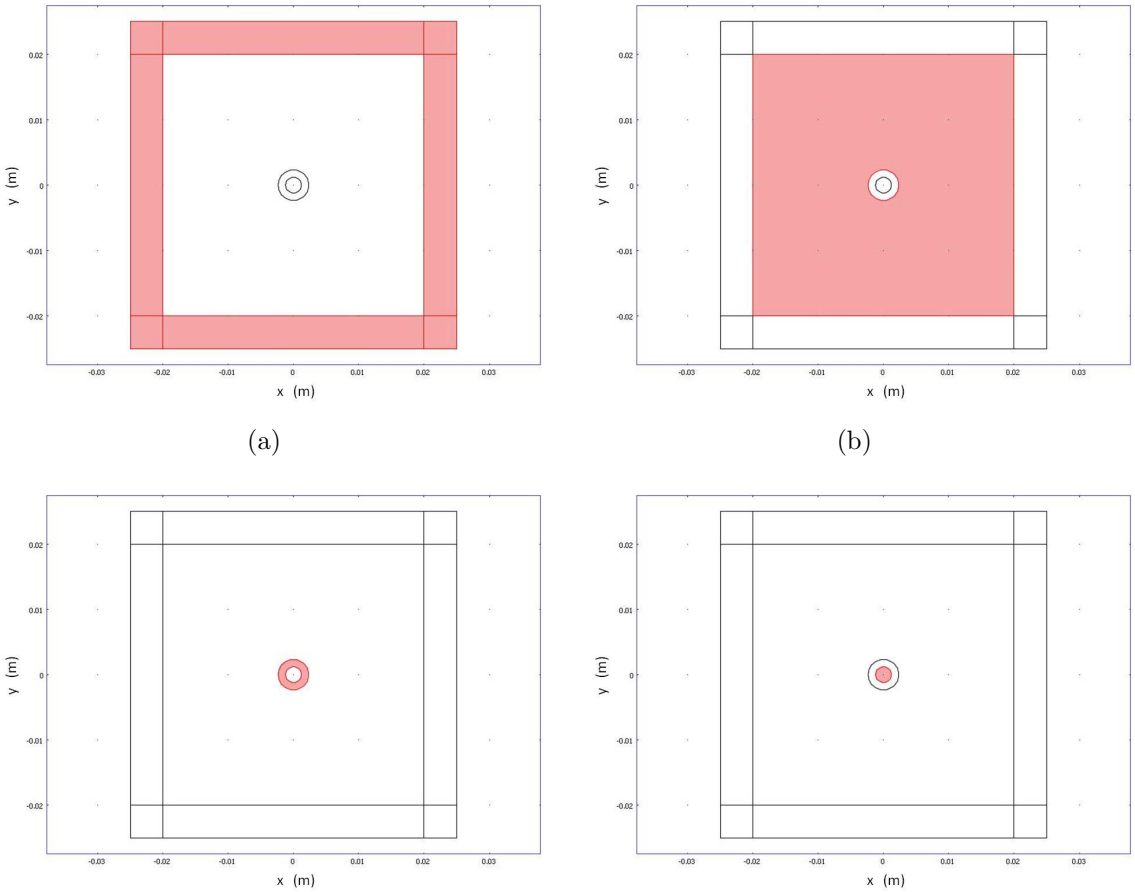

Figure 3.19: Geometry regions defined are (a) perfectly matched layer, (b) free space, (c) dielectric coating, and (d) PEC wire.

inner circle is set to the value of the target's estimated PEC radius. The boundary property of this circle is set to PEC, so the appropriate boundary conditions are applied. Likewise, the radius of the outer circle is set to the estimated dielectric radius. This circle's boundary property is set to ensure a continuous boundary condition is applied. The subdomain properties are set depending on their function. The outer subdomain highlighted in Figure 3.19 (a) is the perfectly matched layer (PML). The PML is required in FEM analysis to absorb the simulated fields without reflecting them. The subdomain in Figure 3.19 (b) is the free space around the target. Because it is free space, the relative permittivity and permeability of this region is 1. The outer

boundary of this subdomain is where the the scattered electric field is converted to its far-field value by COMSOL. The dielectric region is defined by the subdomain highlighted in (c) of Figure 3.19. The properties of this subdomain, the relative permittivity and permeability, are set according to the results of the previous section. The final subdomain is the PEC region, Figure 3.19 (d). Because the boundary of this region is a PEC, no fields exist within this region.

Both TM^z and TE^z solutions can be solved for at the same time because of COMSOL's multiphysics capability. For the TM^z solution, the variable "efarz" contains the complex far-field scattered electric field calculated at every point along the outer boundary of the free-space subdomain. Because the incident electric field has only a $\hat{z}$ component, the scattered field is also $\hat{z}$ oriented. For the TE^z case, the incident electric field is oriented in the $\hat{y}$ direction. The scattered field has both $\hat{x}$ and $\hat{y}$ components. For this reason, the TE^z far-field scattered electric field is a function of the variables "efarx" and "efary". To compare the COMSOL results with the measured 2D RCS of the targets, the data contained in these variables require post-processing to convert them into 2D RCS values. The post-processing is discussed in the numerical model validation section.

3.9 Numerical Model Validation

The far-field data exported by COMSOL is the far-field scattered electric field normalized by the incident field. Since the data is defined along the entire outer boundary of the free-space subdomain, full 360° scattering analysis can be performed. For the purpose of this study, only the data at the monostatic angle, 180°, is required. The incident field is defined propagating in the positive x direction. The far-field data calculated at the center of the left boundary of the free-space subdomain region is the monostatic results. The x, y coordinates are (-0.02,0) referring to the free-space subdomain image in Figure 3.19 (b). The "efarx", "efary", and "efarz" variables are exported into a ".txt" file. The ".txt" files are imported into Matlab® and the monostatic data is extracted for conversion. The TM^z and TE^z 2D RCS conversions

are

$$\sigma_{2D_{comsol}}^{TM^z} = 2\pi\lambda \left|\text{efarz}\right|^2 \tag{3.18}$$

$$\begin{aligned}\sigma_{2D_{comsol}}^{TE^z} &= 2\pi\lambda \left|\hat{x}\ \text{efarx} + \hat{y}\ \text{efary}\right|^2 \\ &= 2\pi\lambda \left(\sqrt{|\text{efarx}|^2 + |\text{efary}|^2}\right)^2 \\ &= 2\pi\lambda \left(|\text{efarx}|^2 + |\text{efary}|^2\right) \ .\end{aligned} \tag{3.19}$$

The data exported by COMSOL is normalized by the wavelength, λ, so the data must be factored by λ in the conversion. The factor, 2π, is from the definition of the 2D RCS, equation (2.4). In equation (3.19), the scattered field is separated into its orthogonal components. To get the magnitude, they are added in quadrature. For the TE^z case, COMSOL uses the magnetic field, **H**, as the incident wave. To ensure the correct amplitude is used for the electric field, the amplitude of the magnetic field, H_o, must be E_o/η where E_o is the amplitude of the electric field and η is the intrinsic impedance of the medium. For this case, the medium is free-space. The intrinsic impedance of free-space, denoted by η_o, is $\approx 377\Omega$ [5].

In the previous section, the concept of meshing is shown to define the entire region to be analyzed. The degree of accuracy of a FEM analysis is dependent on the maximum length of the mesh elements. If the region is not meshed adequately, the results are less accurate. Figure 3.20 shows the the resulting 2D RCS of three different COMSOL default mesh qualities compared with the exact solution of a PEC with a radius of 1.2 mm. The mesh requirements differ between the TM^z and TE^z cases for this example. When it comes to meshing, the more mesh elements in the model means the more accurate the solution is and the longer the model takes to run.

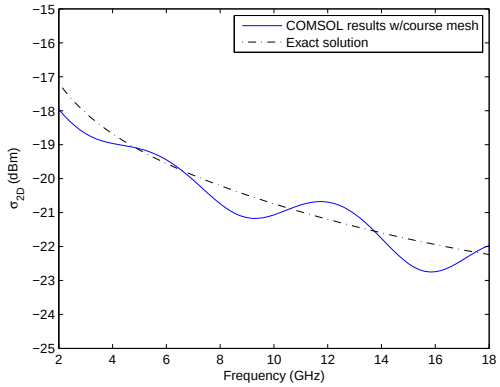

(a)

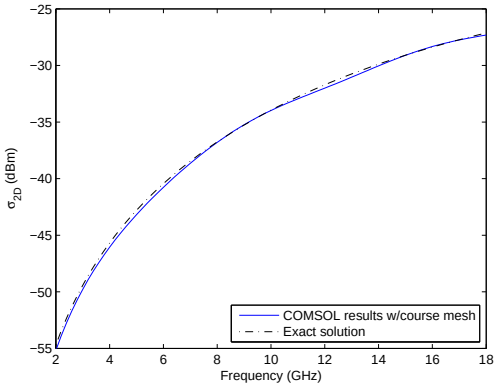

(b)

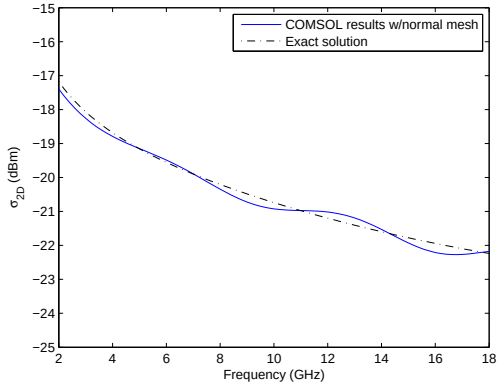

(c)

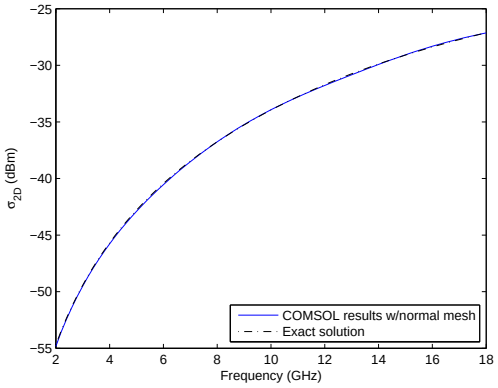

(d)

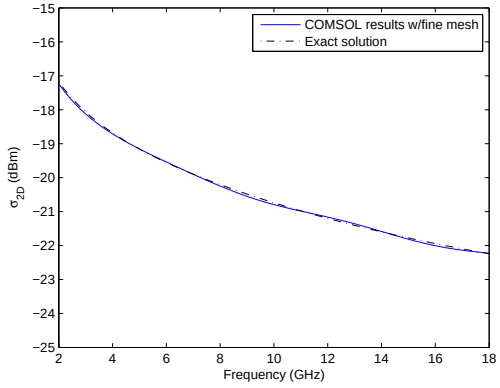

(e)

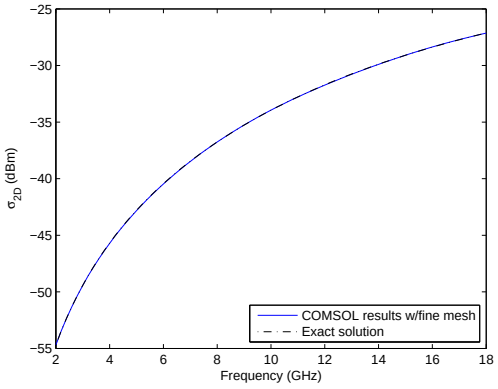

(f)

Figure 3.20: The 2D RCS of a PEC cylinder with a radius of 0.0012 mm using different levels of meshing. (a) Course mesh (TM^z), (b) course mesh (TE^z), (c) normal mesh (TM^z), (d) normal mesh (TE^z), (e) fine mesh (TM^z), and (f) fine mesh (TE^z).

IV. Data/Analysis Discussion

The goals of this research effort are to determine the 2D RCS of data-linked support strings, determine the material properties of the string material, and accurately model the data-linked support strings as single cylindrical wires uniformly coated with a simple dielectric coating. The term simple refers to the dielectric coating being linear, homogeneous, isotropic and non-dispersive. The previous chapter details the processes to achieve these goals. The targets' scattering parameters are measured with the GTRI focus beam system and amplitude corrected to determine the 2D RCS from 2 to 18 GHz. From the measurements, an attempt to determine the effective relative permittivity of the string material is made. The estimated effective relative permittivity is then used to build a simple dielectric-coated wire model in COMSOL for analysis. Finally, the COMSOL results are compared to the measurement results to verify the accuracy of the simple model. This chapter provides the results of these efforts in the following sections. The first section is the results from the measurement process.

4.1 Focus Beam Measurement Results

As stated in Subsection 3.3.3, each target is measured a total of 5 times. The targets are physically removed from the frame and set up again in an effort to capture the set-up error introduced into the measurements. Also, the portion of the target measured is varied between measurements. This is another source of error if the wire positions within the strength member varies along the length of the string. Both of these errors are lumped together in the variability analysis. Figures 4.1 and 4.2 show the squared magnitude of the scattering parameters of each target for TM^z and TE^z polarization respectively.

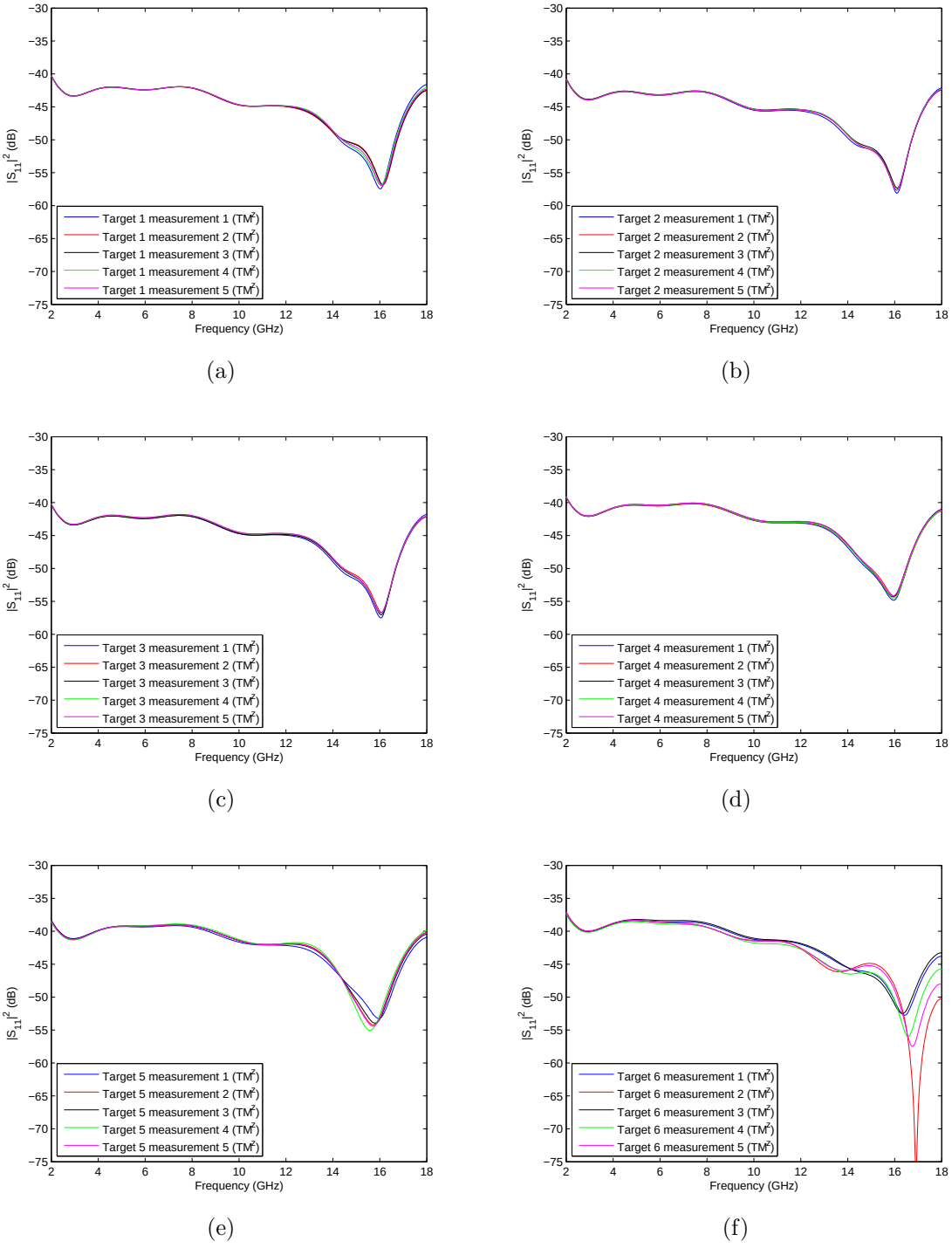

Figure 4.1: Repeated TM^z measurements of (a) target 1, (b) target 2, (c) target 3, (d) target 4, (e) target 5, and (f) target 6.

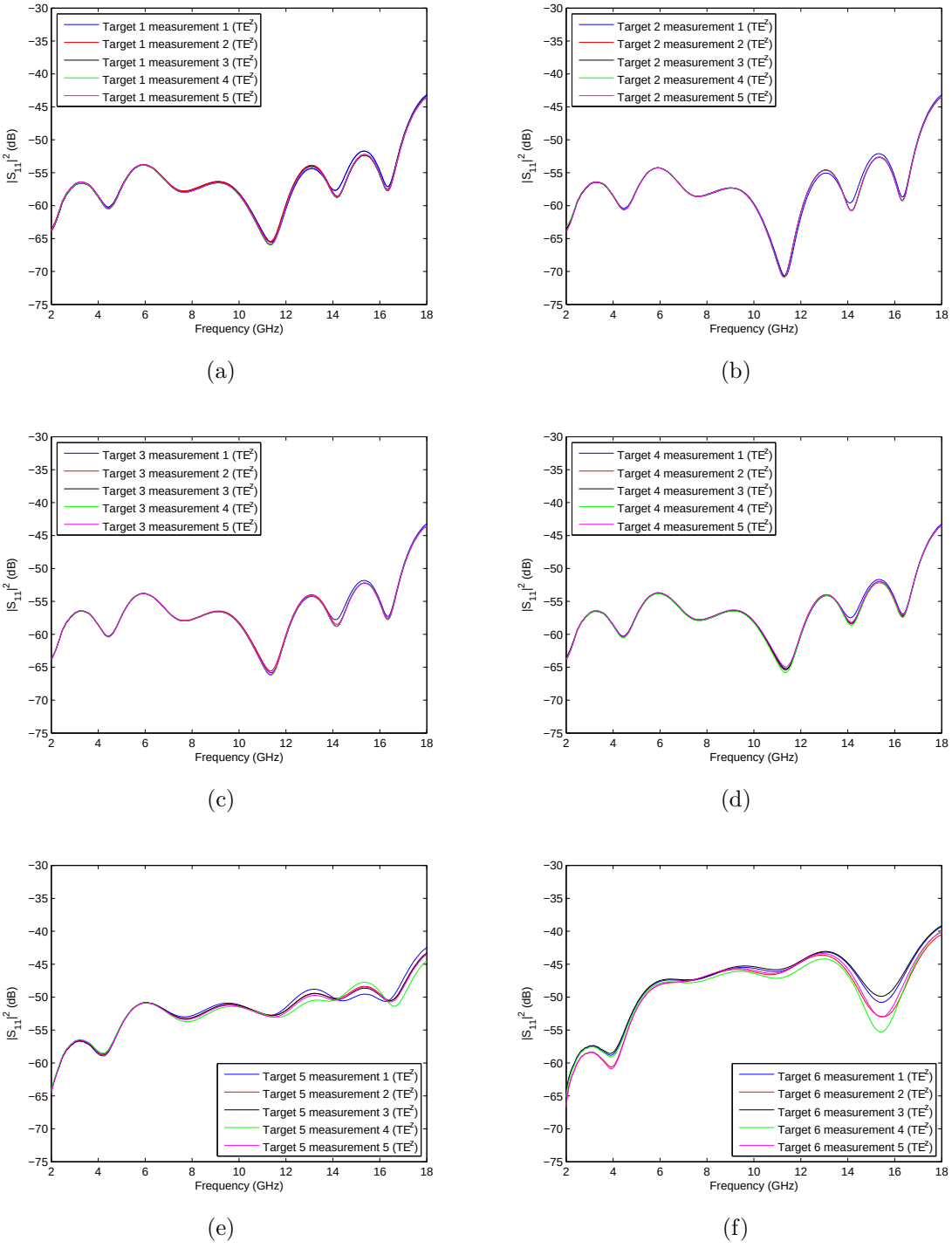

Figure 4.2: Repeated TE^z measurements of (a) target 1, (b) target 2, (c) target 3, (d) target 4, (e) target 5, and (f) target 6.

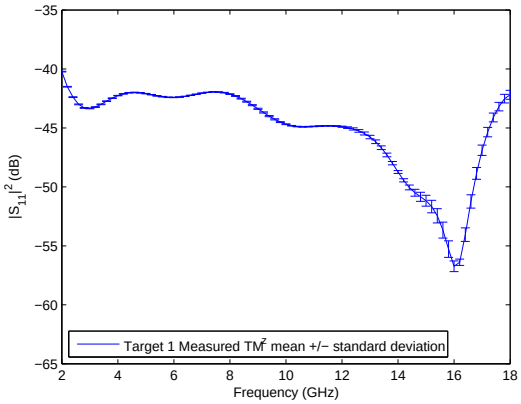

(a)

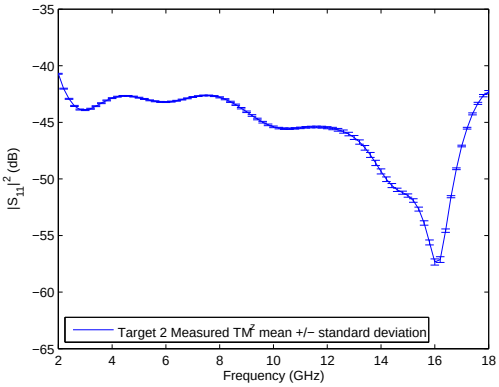

(b)

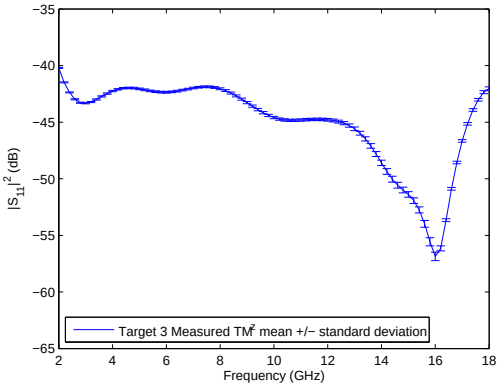

(c)

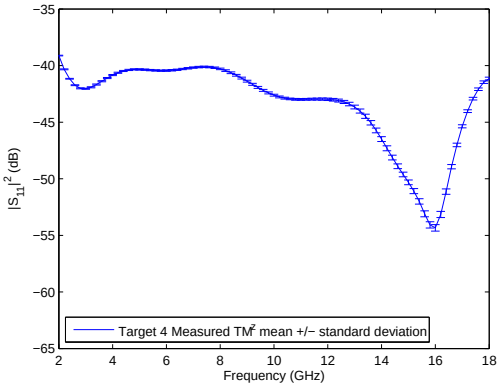

(d)

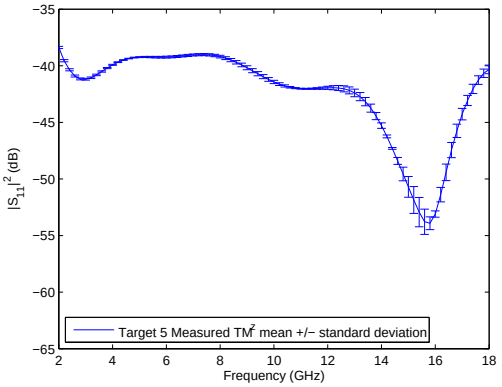

(e)

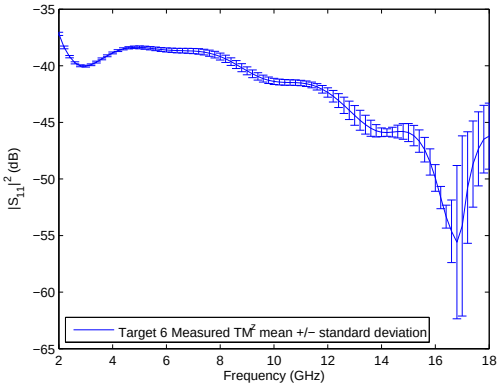

(f)

Figure 4.3: TM^z measurements averaged with one standard deviation errorbars for (a) target 1, (b) target 2, (c) target 3, (d) target 4, (e) target 5, and (f) target 6.

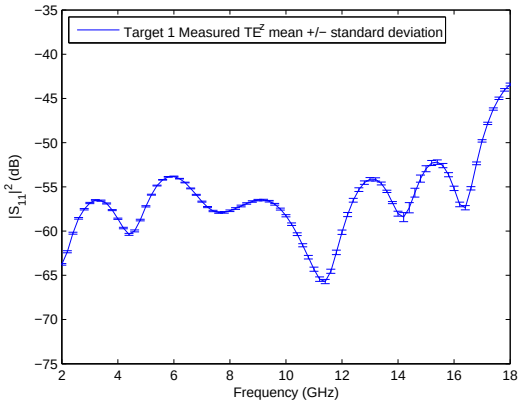

(a)

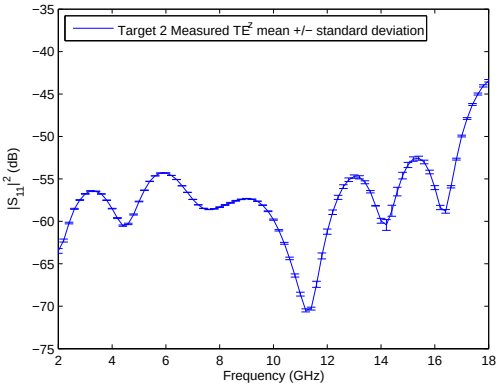

(b)

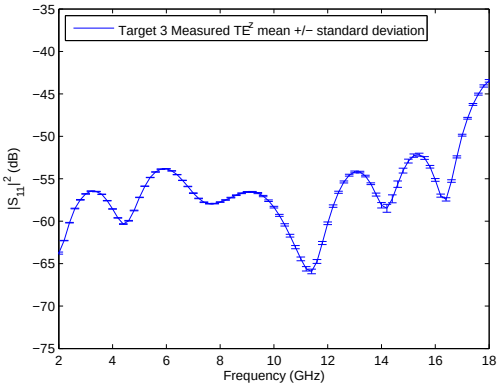

(c)

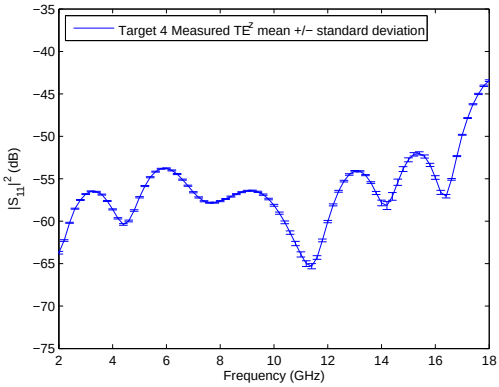

(d)

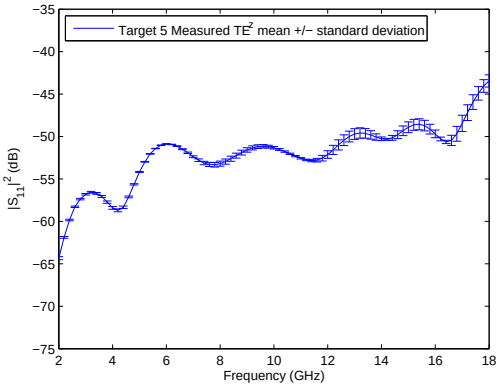

(e)

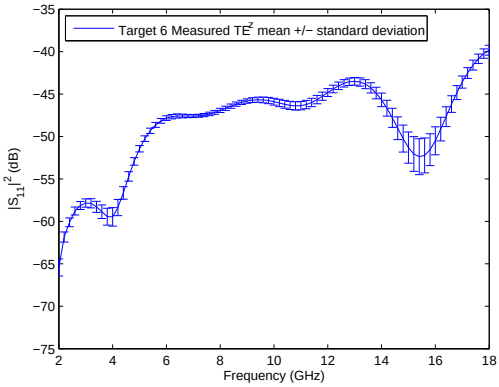

(f)

Figure 4.4: TE^z measurements averaged with one standard deviation errorbars for (a) target 1, (b) target 2, (c) target 3, (d) target 4, (e) target 5, and (f) target 6.

The variability associated with set-up is expected to be small due to the stable measurement structure. Relatively short samples are required and are mounted to a rigid target frame. The misalignment error induced by not repeatedly mounting the target in the same position is small because the target frame contains a built in ruler facilitating accurate target positioning. As seen in Figures 4.1 and 4.2, targets 1-4 measurements are stable from measurement to measurement. Targets 5 and 6 measurements are less stable especially at frequencies above 10 GHz. Targets 5 and 6 are common conducting wires. Their wire core is more susceptible to deformation due to kinking and flattening. The effort is made to make them as straight as possible for each measurement. To the naked eye, they seem straight, but it is apparent there is more error associated with these two targets based on the results in Figures 4.1 and 4.2. A useful characterization of the measurement statistics is the standard deviation. The standard deviation quantifies the "spread" of the measurements [19]. Figures 4.3 and 4.4 plot the average of the 5 measurements with the error bars at $\pm$ 1 standard deviation calculated in the dB domain. These plots show for the data-linked string samples, the measurements are very repeatable using the GTRI focus beam system. After the measurement data is obtained, the data is corrected.

The first step of the correction process is coherent background subtraction. This removes the background clutter within the time gate from the target data. The assumption is the background remains unchanged for all of the target measurements. If the scene is dramatically changed between the background measurement and the target measurement, background subtraction as a method of improving the quality of the target data breaks down. To prevent this, special care is taken not to disturb the scene throughout the entire data collection. A way to determine if the background measurement taken at the beginning of the collection changes significantly is to take a background measurement at the end of the collection and compare the two. Figure 4.5 shows the measured background remained very stable under 10 GHz for both polarizations.

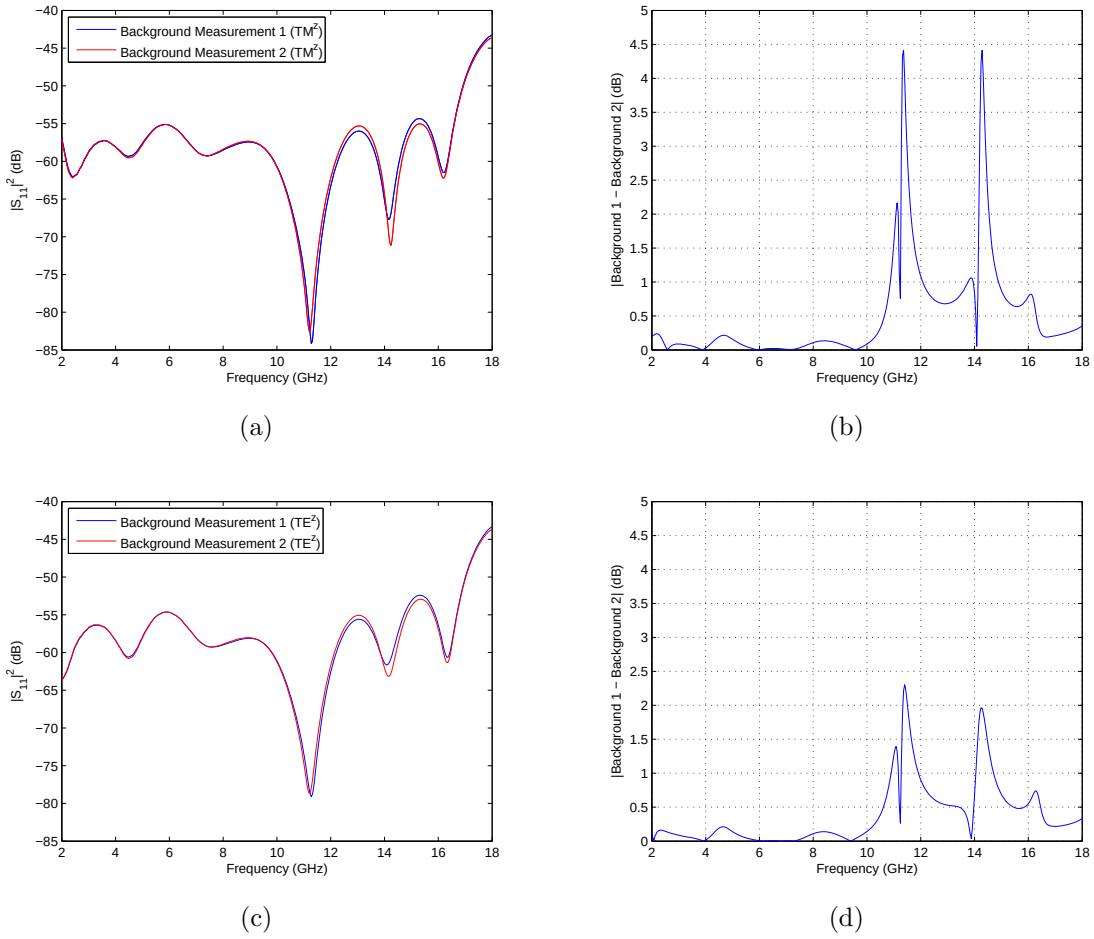

Figure 4.5: Comparison of background measurement taken before measuring targets and after. (a) TM^z, (b) difference between two background measurements (TM^z), (c) TE^z, and (d) difference between two background measurements (TE^z).

After background subtraction, the data is amplitude corrected by measuring a target with a known response and comparing the measured response to the expected response. This technique is analogous to channel characterization in communication theory. In this case, the reference target is a 1/4-in diameter aluminum rod. The reference target is used to correct the measured data of a 1/2-in diameter aluminum rod. The corrected 2D RCS of the 1/2-in target is compared to its exact expected value. The results for both the TM^z and TE^z data corrections are shown in Figure 4.6. The degree of accuracy throughout the entire frequency range is extremely good

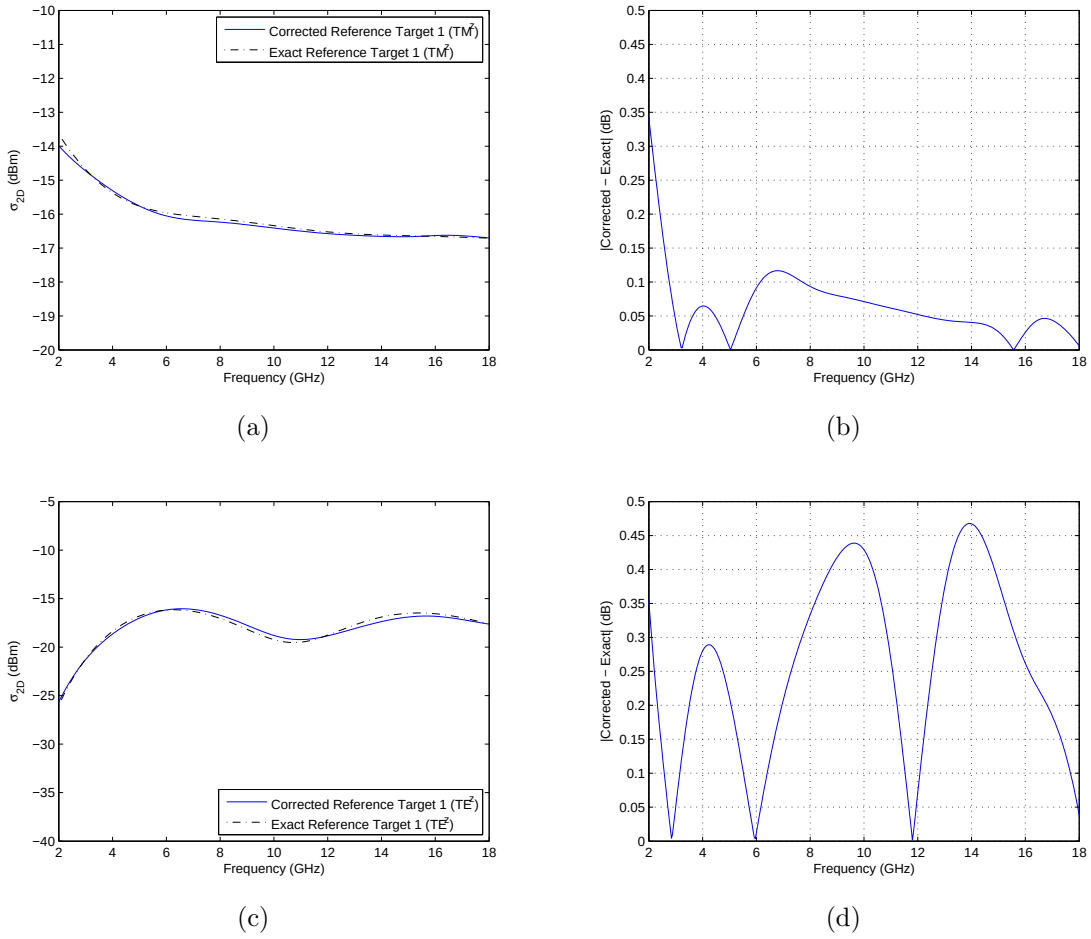

Figure 4.6: Comparison of the corrected 2D RCS of reference target 1 (a) corrected 2D RCS and exact for TM^z, (b) difference between corrected and exact TM^z, (c) corrected 2D RCS and exact for TE^z, and (d) Difference between corrected and exact TE^z.

with a maximum difference less than 0.5 dB. The measured data of each target is corrected using the 1/4-in rod, as the reference target. The corrected results are shown in Figure 4.7 for both TM^z and TE^z 2D RCS's. Target 2 has the lowest 2D RCS for both cases. This is not surprising since it is the thinnest string sample with the thinnest wires. Expectedly, target 6, the largest of the targets, has the strongest 2D RCS for both cases. Over most of the frequency range, the 2D RCS of the targets behaves in a stable manner. Due to the consistent drop-off observed in Figure 4.7 (b)

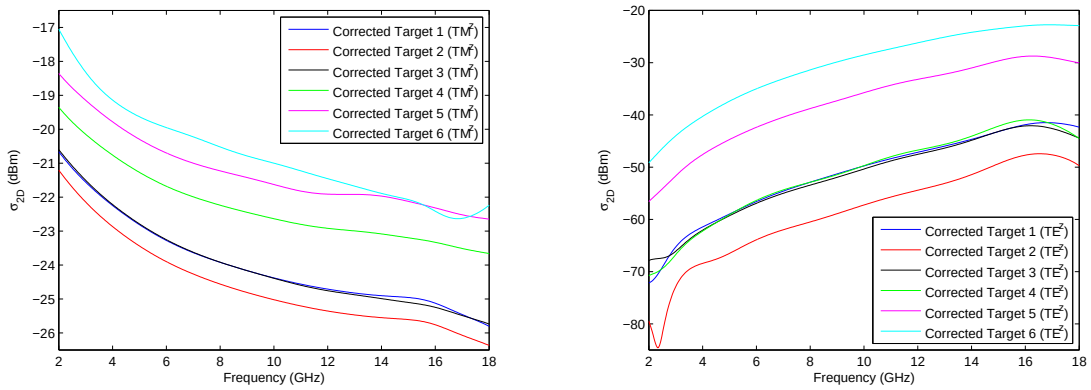

(a) (b)

Figure 4.7: The measured 2D RCS's of each target for (a) TM^z and (b) TE^z.

for targets 1-4 below 3 GHz, the TE^z 2D RCS of the data-linked strings below 3 GHz looks to be at the lower limit of the the focus beam's sensitivity.

4.2 Dielectric Constant Search Results

Recall the assumptions from Section 3.7. It is assumed the string strength member has a relative permeability of 1 and the relative permittivity is purely real. Figure 4.8 shows the effect of changing the relative permittivity of the target 6 model for both polarizations. The TM^z 2D RCS is not very sensitive to small changes in the dielectric constant. Figure 4.8 shows the change in the 2D RCS is less than 1 dB when the dielectric constant is changed from 1 to 7.5 at 18 GHz. The expected ε_r values for the strength members are no more than 5 based on Table 2-1 in Balanis [5]. Using the TM^z 2D RCS is not practical for very thin targets with thin dielectric thicknesses. Analogous to thin film interference studied in optics, it is not until the electrical thickness of the dielectric material facilitates strong interference (destructive or constructive) between the scattered wave from the dielectric and the scattered wave from the PEC core that using the TM^z 2D RCS becomes practical. From Figure 4.9,

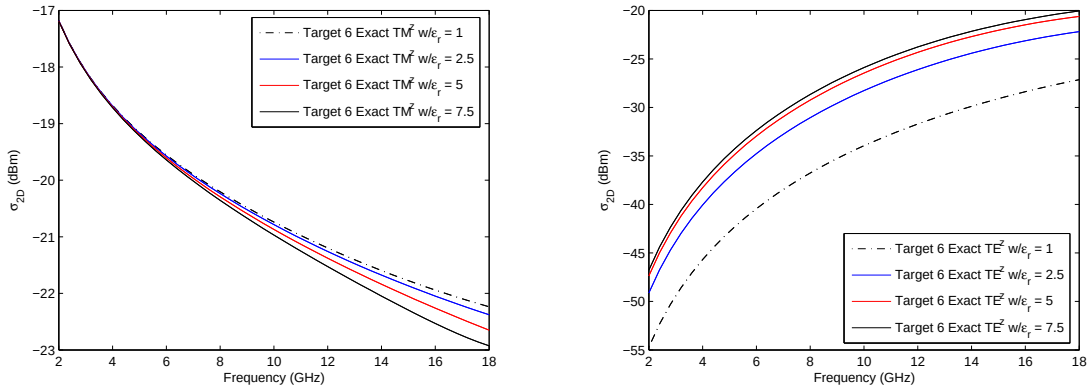

(a) (b)

Figure 4.8: (a) TM^z 2D RCS not sensitive to small changes in dielectric constant and (b) TE^z 2D RCS sensitive to small changes in dielectric constant

the phase difference between the two reflections,

$$\begin{aligned} \delta\theta &= \beta_d \, 2(b-a) \\ &= 2\pi f \sqrt{\varepsilon_o \mu_o} \, \sqrt{\varepsilon_r} \, 2(b-a) \ , \end{aligned} \tag{4.1}$$

is a function of the thickness and relative permittivity of the dielectric coating and the frequency, f, of the incident wave. The π phase shift from the PEC is negated by the π phase shift at the dielectric. Destructive interference is experienced when $\delta\theta = (2n+1)\pi$, where n is an integer. Likewise, constructive interference is experienced when the phase difference is an integer multiple of 2π. For the case when ε_r is 7.5 in Figure 4.8 (a), the first null due to destructive interference is not expected until approximately 24.3 GHz, which is outside of the frequency range of the GTRI focus beam configuration used for this study.

However, the TE^z 2D RCS is very sensitive to small changes in the dielectric constant. Figure 4.8 (b) shows an approximate 5-dB increase in the 2D RCS when the dielectric constant is changed from 1 to 2.5. Consider the ratio of the radius of the target's PEC core to the wavelength of the incident wave. For target 6, the largest target with a PEC radius of 1.2 mm, the ratio at 18 GHz, the shortest wavelength, is

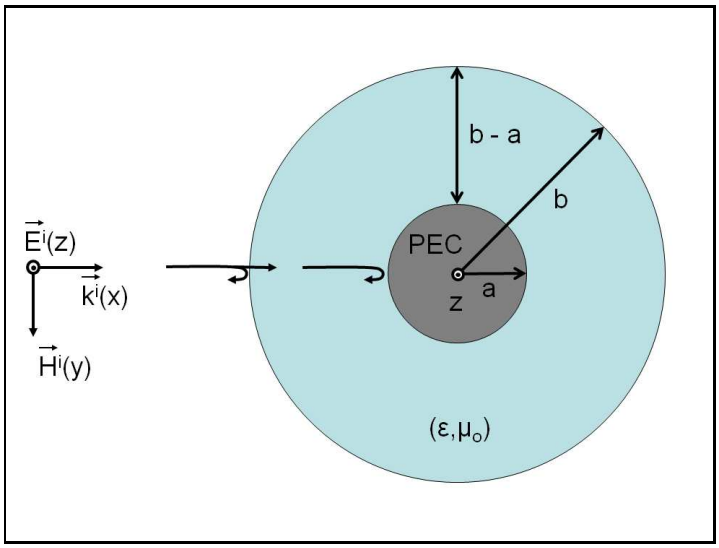

Figure 4.9: Equation (4.1) illustration.

approximately 0.072. The rest of the targets have smaller ratios. This is referred to as the low-frequency scattering regime [16] where the wavelengths are much longer than the physical extent of the target. This produces a "quasi-static" field with very little phase change along the target surface. At any instant in time, the target has surface charges separated according to the incident electric field's direction. This results in a dipole moment. The definition of a dipole moment is charge density multiplied by the distance between the charges. The dipole moment concept is illustrated in Figure 4.10. Consider a simple atom model with a positively charged center due to protons, p^+, at the nucleus. Orbiting around the nucleus are negatively charged electrons, e^-. For this case, the electron is bound to the atom meaning it is not free to leave the atom like those of conductors. The left side of Figure 4.10 (a) illustrates this model. Without an applied electric field, the atom is locally neutral. With an electric field applied, the right side of Figure 4.10 (a), the orbit of the electron is distorted or aligned with the electric field. This causes an effective dipole moment at the atomic level. This dipole moment is infinitesimally small. A dielectric material is a material consisting of bound electrons. With an applied electric field, the atomic dipoles have a cumulative effect. Within the dielectric region, the net effect of neighboring dipoles cancel due to positive and negative charges in close proximity. However, at the surface of the dielectric, the

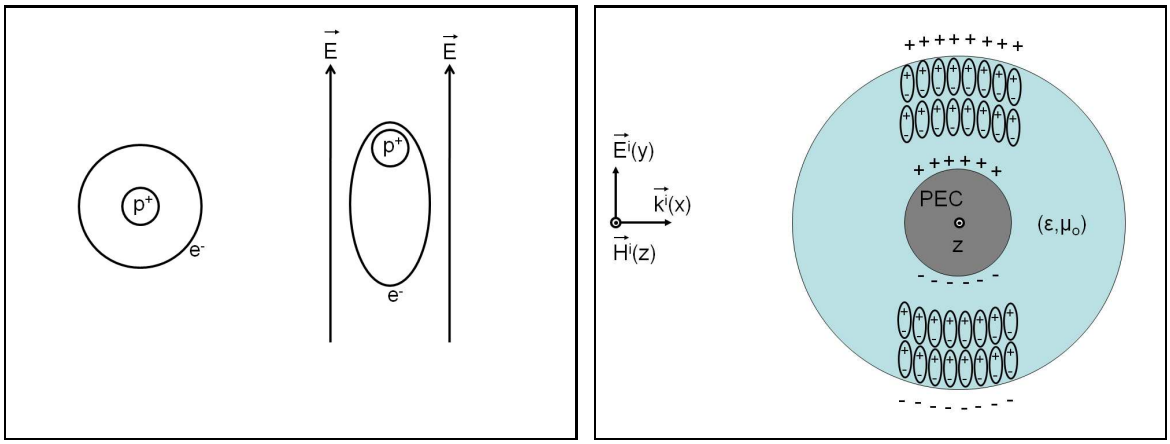

(a) (b)

Figure 4.10: (a) Simple model of atom without and with an applied electric field [5] and (b) dielectric-coated wire in "quasi-static" electric field setting up dipole moment.

polarization charges "build up" because there are no opposite charge to cancel with. The polarization surface charge, q_{ps}, is defined as $\hat{n} \cdot (\varepsilon_2 \mathbf{E}_2 - \varepsilon_1 \mathbf{E}_1) = q_{ps}$ [5], where the subscript 2 is the free space region and subscript 1 is the dielectric region. The overall effect is a a dipole moment with a separation distance equal to the diameter of the dielectric. On the surface of the PEC within the dielectric material, electron surface charge, q_{es}, builds up according to $\hat{n} \cdot \varepsilon_1 \mathbf{E}_1 = q_{es}$ [5] and is separated by the diameter of the PEC setting up another dipole moment. Figure 4.11 shows this concept visually. Target 6 is modeled with six different relative permittivity values, 1-6. Figure 4.11 (a), $\varepsilon_r = 1$, shows the magnitude of the total electric field attached to the PEC from which the surface charge can be calculated. The arrows represent an arrow plot of the scattered electric field. From inspection, the arrows display the classic dipole shape. As the relative permittivity is increased, the coexistence of two dipoles is apparent. The two dipole moments can be represented by one effective dipole moment. Finally, the dielectric constant increases to a point where the surface charge on the PEC becomes negligible due to the increasing dipole strength within the dielectric. Eventually, the the only dipole moment is the dipole moment associated with the polarization surface charge on the dielectric material.

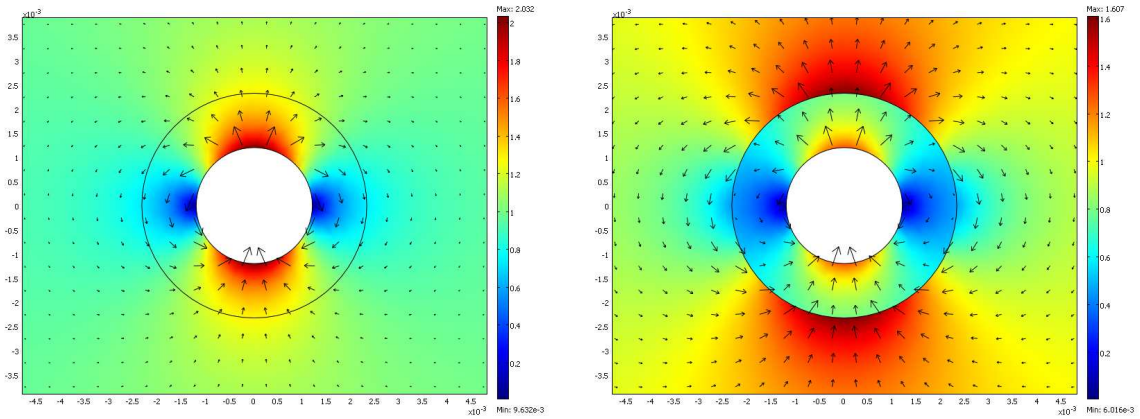

(a) (b)

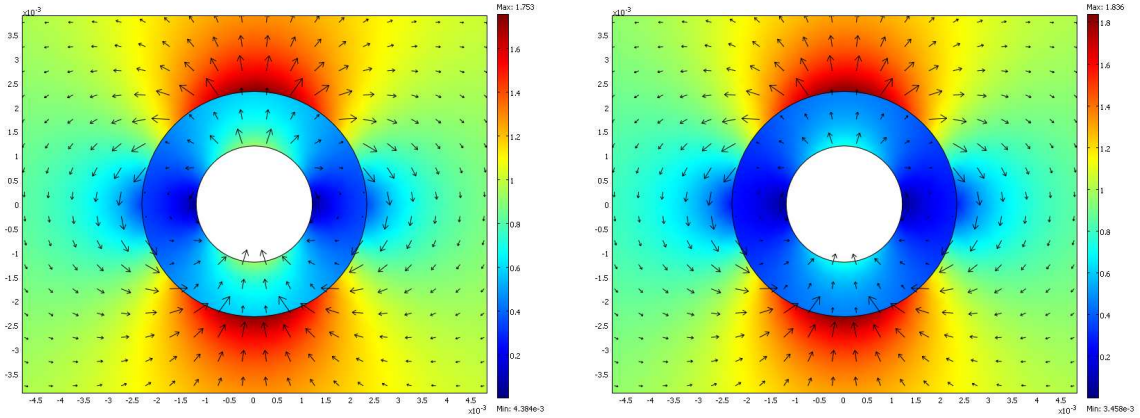

(c) (d)

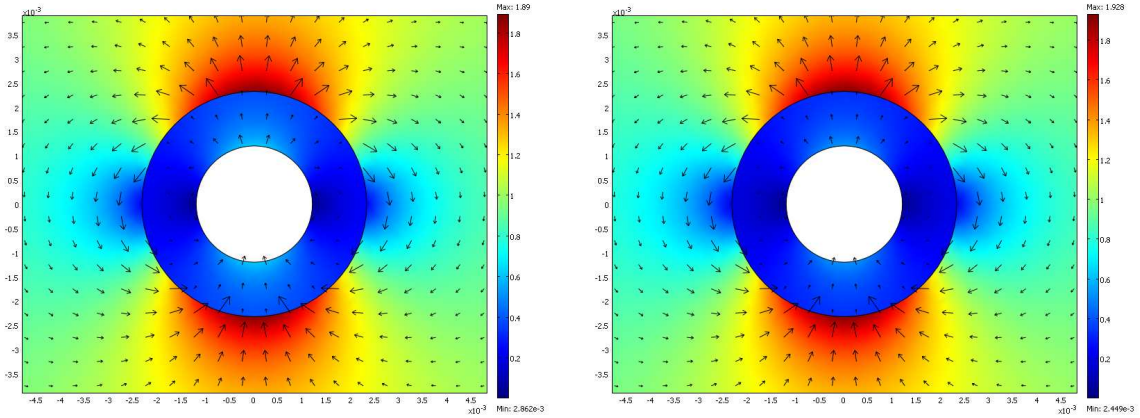

(e) (f)

Figure 4.11: Dipole moments due TE^z illumination of target 6 with (a) $\varepsilon_r = 1$, (b) $\varepsilon_r = 2$, (c) $\varepsilon_r = 3$, (d) $\varepsilon_r = 4$, (e) $\varepsilon_r = 5$, and (f) $\varepsilon_r = 6$.

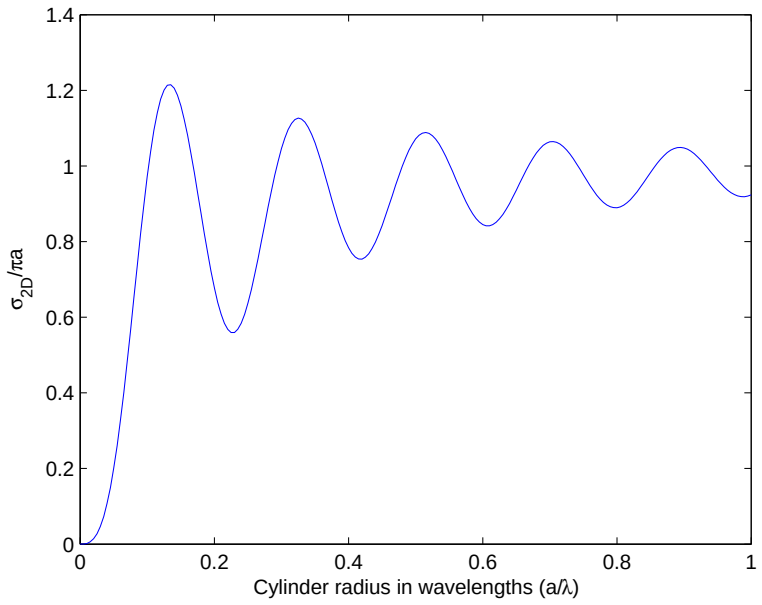

Figure 4.12: Normalized 2D RCS of PEC cylinder vs. ratio of cylinder radius to wavelength.

The 2D RCS as a function of the dipole moment is the Rayleigh region ($a/\lambda < 0.1$) of Figure 4.12. This region ($a/\lambda \leq 0.1$) is characterized by the linear relationship between the 2D RCS and the ratio of the radius to wavelength. The steep slope indicates a large change in the 2D RCS to a small change in the ratio. Thus, using the TE^z 2D RCS to determine the effective relative permittivity of the targets is the best choice. Recall from Figure 4.8 (b), the TE^z 2D RCS increases as the dielectric constant increases. Figure 4.13 shows each target's 2D RCS and the theoretical 2D RCS of the target with a dielectric constant of 1. The error minimization algorithm to find ε_r of a target begins with an air dielectric and increases the dielectric constant until the model's 2D RCS matches the measured 2D RCS for each frequency. The resulting values of ε_r are plotted vs frequency in Figure 4.14.

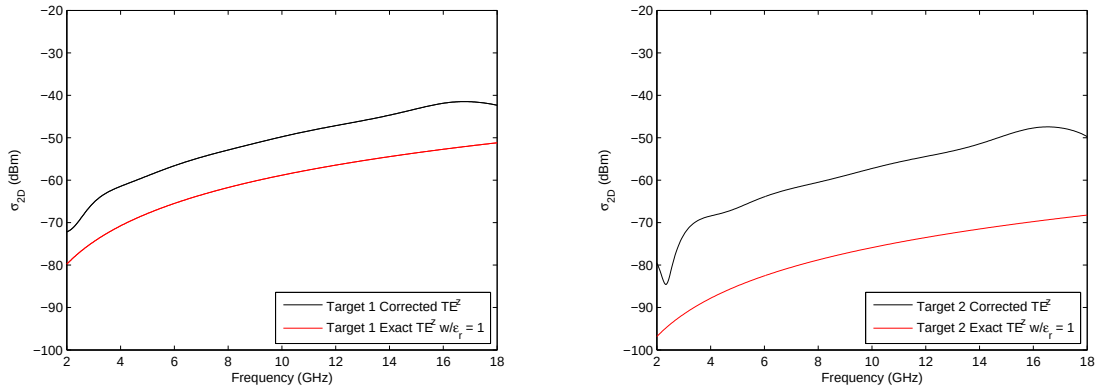

(a)

(b)

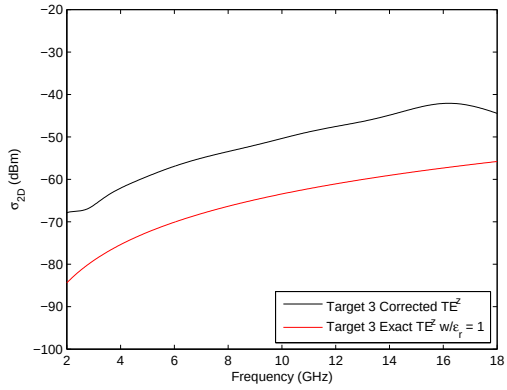

(c)

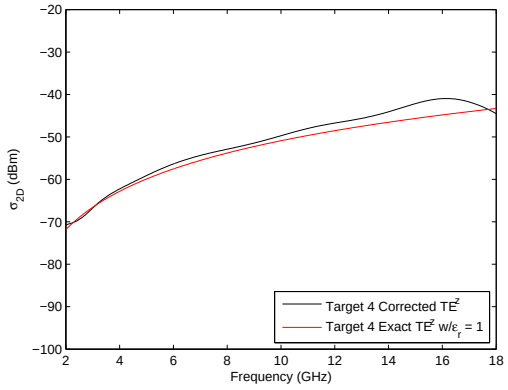

(d)

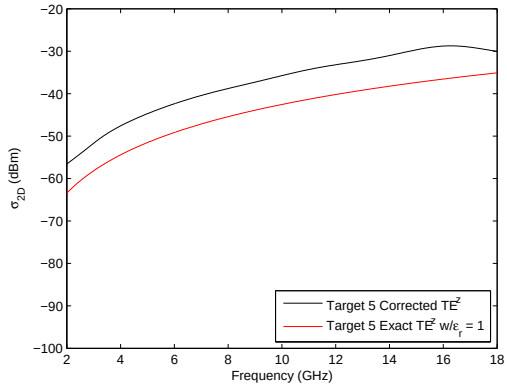

(e)

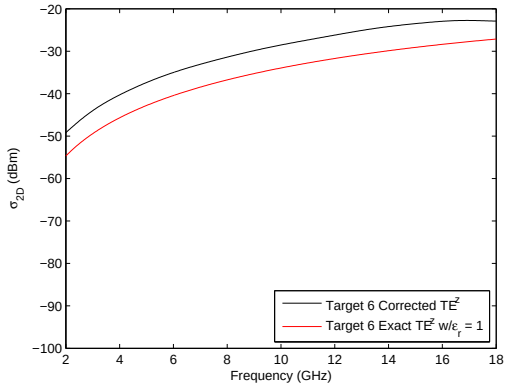

(f)

Figure 4.13: TE^z 2D RCS of targets compared to theoretical target with air dielectric for (a) target 1, (b) target 2, (c) target 3, (d) target 4, (e) target 5, and (f) target 6.

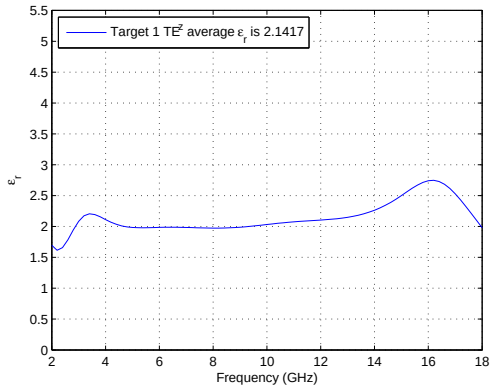

(a)

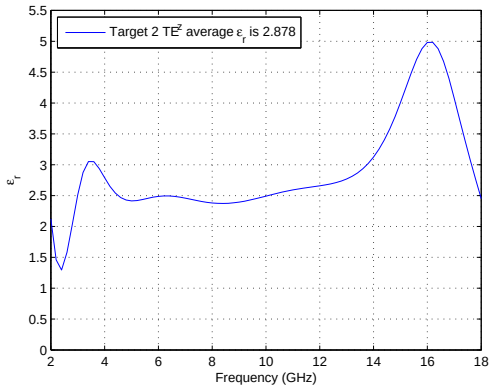

(b)

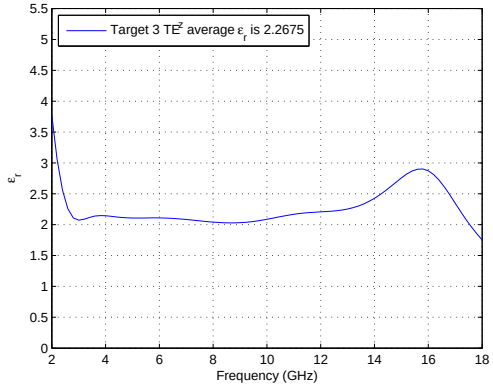

(c)

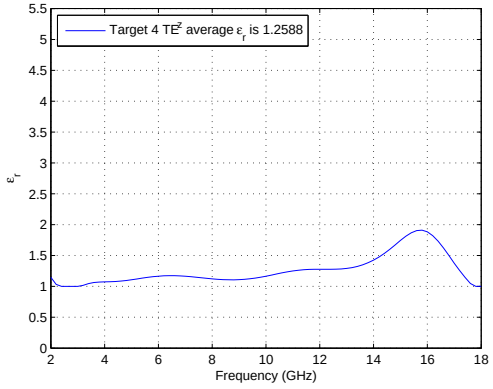

(d)

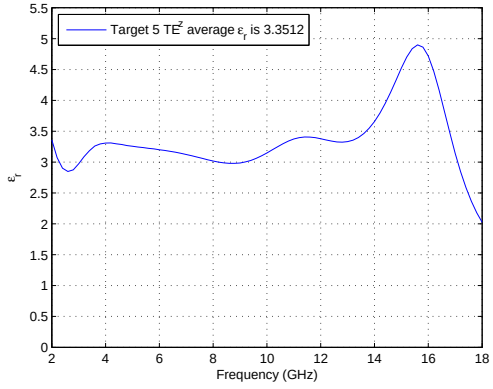

(e)

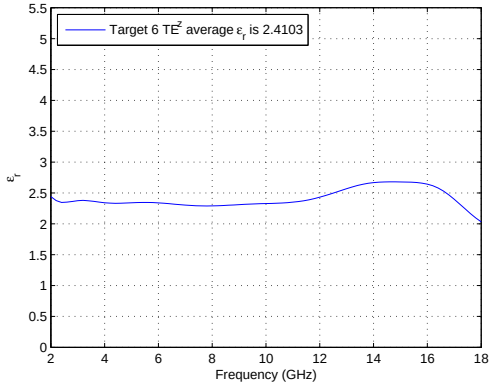

(f)

Figure 4.14: Results of ε_r search for (a) target 1, (b) target 2, (c) target 3, (d) target 4, (e) target 5, and (f) target 6.

The values obtained are within the expected range of dielectric constants. The results are most consistent from 5 GHz to 11 GHz and are re-averaged over that range to get the value for the COMSOL model. The new averages are shown in Table 4.1.

Table 4.1: Average ε_r between 5-11 GHz

Target	Average ε_r (5-11 GHz)
Target 1	1.999
Target 2	2.454
Target 3	2.083
Target 4	1.152
Target 5	3.136
Target 6	2.321

The next step is to use these values for the dielectric sub-domain in the COMSOL model and compare those results with the measured 2D RCS.

4.3 COMSOL Results

Figures 4.15, 4.16, and 4.17 show the comparisons between the measured 2D RCS and COMSOL analysis of the simple dielectric-coated wire model results for both polarizations. The agreement is good by visual inspection. A measure of accuracy is the mean squared error (MSE) between the two results. Table 4.3 shows the computed MSE's between the two curves for each target and polarization over the entire frequency range, 2-18 GHz. The simple dielectric-coated model is a good

Table 4.2: MSE between measured 2D RCS and COMSOL results

Target	TM^z MSE	TE^z MSE
Target 1	0.037 dB	2.108 dB
Target 2	0.822 dB	3.730 dB
Target 3	0.022 dB	1.172 dB
Target 4	0.103 dB	1.382 dB
Target 5	0.148 dB	0.243 dB
Target 6	0.075 dB	0.073 dB

approximation for the complex structure of the sample data-linked support strings for

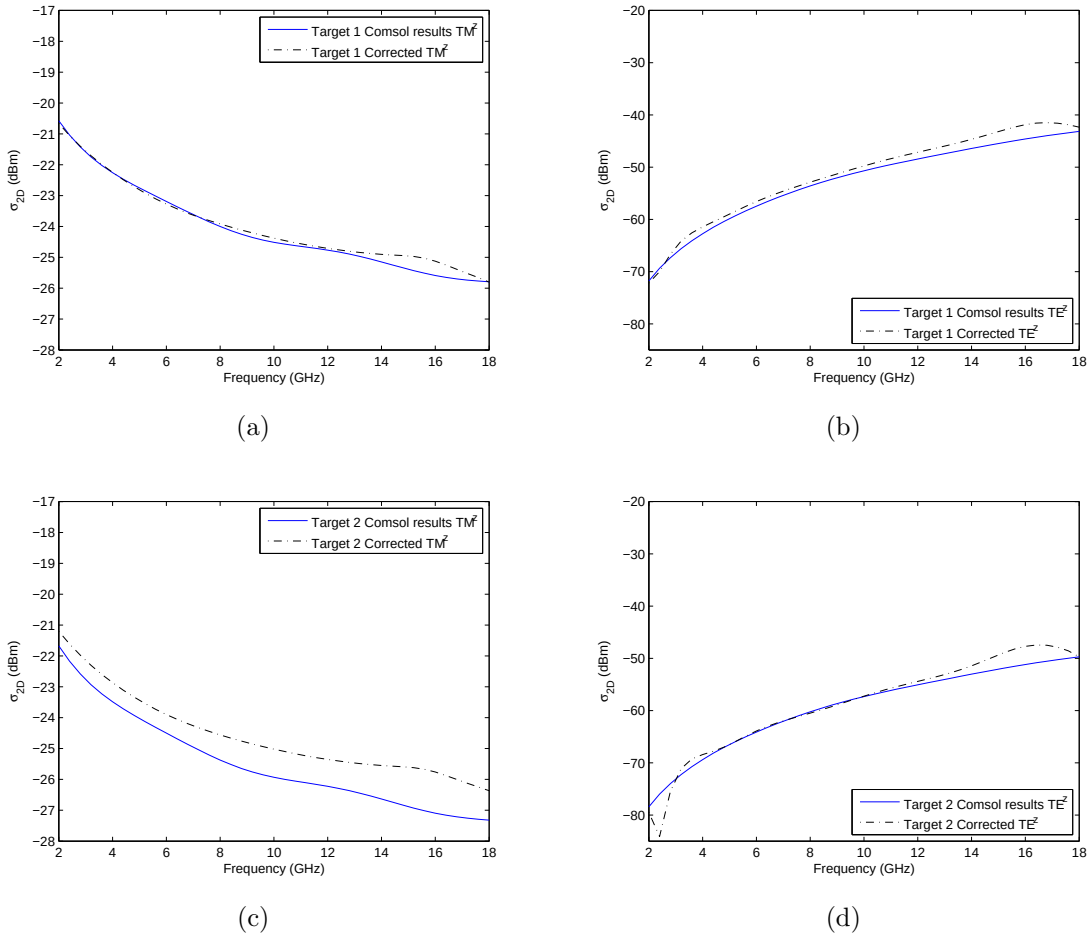

Figure 4.15: Comparison of COMSOL results to measured 2D RCS for (a) target 1 (TM^z), (b) target 1 (TE^z), (c) target 2 (TM^z), and (d) target 2 (TE^z).

2D scattering analysis. This provides a convenient representation for future modeling efforts. The accuracy of the model may be improved with an iterative effort to better estimate the variables of the model.

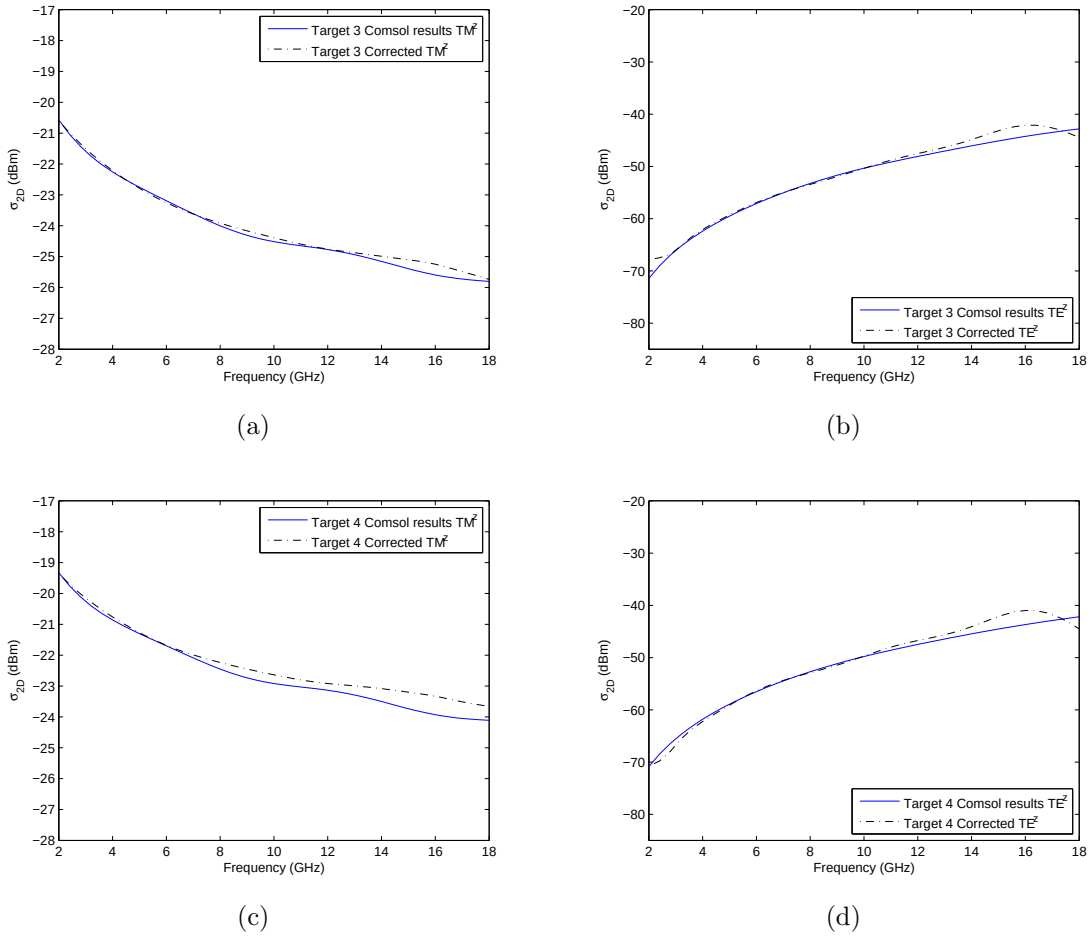

Figure 4.16: Comparison of COMSOL results to measured 2D RCS for (a) target 3 (TM^z), (b) target 3 (TE^z), (c) target 4 (TM^z), and (d) target 4 (TE^z).

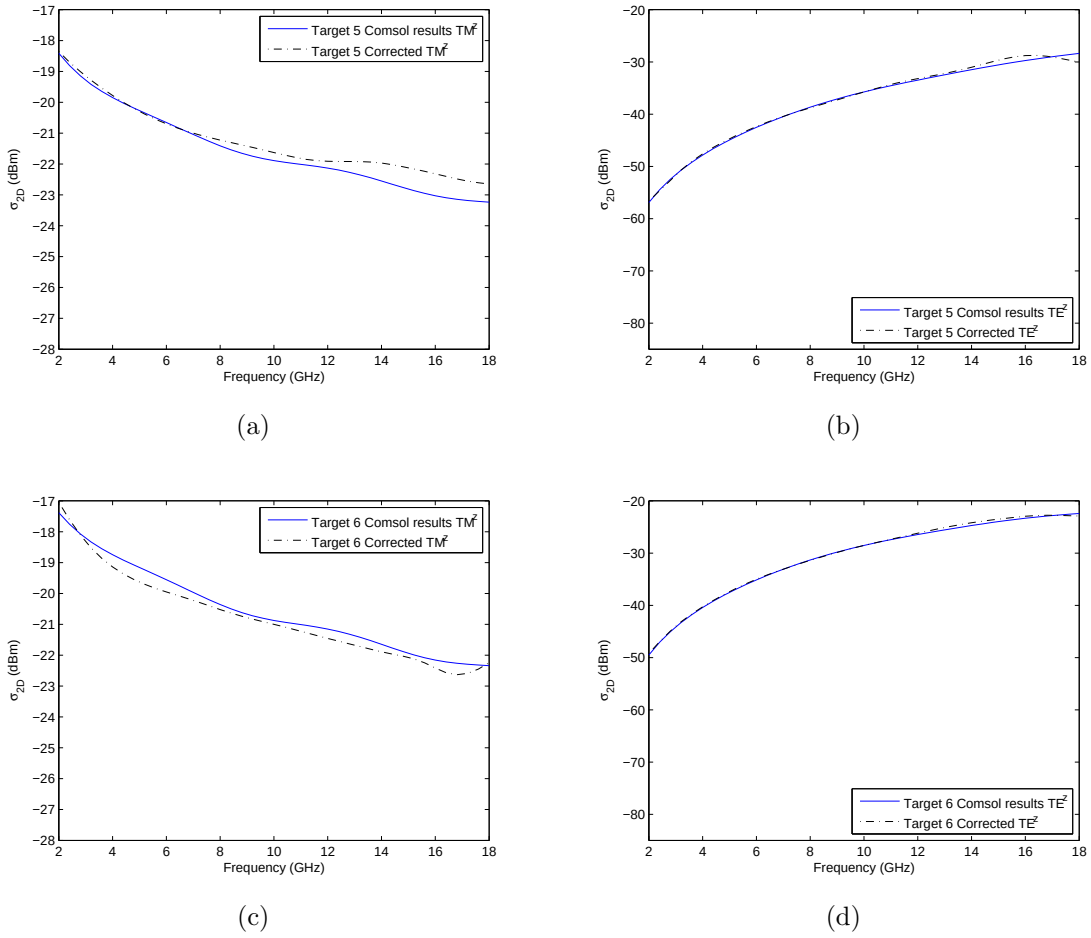

Figure 4.17: Comparison of COMSOL results to measured 2D RCS for (a) target 5 (TM^z), (b) target 5 (TE^z), (c) target 6 (TM^z), and (d) target 6 (TE^z)

V. Conclusions

Interest in the bistatic RCS of aircraft is growing. To improve indoor bistatic RCS measurements by removing the bistatic antenna support apparatus, a data-linked string supported bistatic measurement system is proposed as a potential solution. To this end, candidate data-linked strings are analyzed.

5.1 Summary

The main objective of this research was to determine the scattering properties of four data-linked support string samples. Another goal was to determine the material properties of the string material through nondestructive means. The final goal was to model the samples as a single wire coated with a dielectric material and determine the validity of the model. At the beginning of this thesis, the following questions were presented:

1. Given some samples, what is the clutter contribution of each sample?
2. Can accurate scattering analysis be performed with a focus beam system?
3. What are the scattering mechanisms associated with the samples?
4. Can the constitutive parameters of the samples be determined through nondestructive evaluation?
5. Can the strings be accurately modeled as a single wire with a dielectric coating for numerical analysis?

To answer these questions, the two dimensional radar cross section of each sample was measured with a focus beam system. The resulting measurements were used in conjunction with an analytic model of a dielectric-coated wire to estimate the material properties of the strings. Finally, a dielectric-coated wire model for each sample was analyzed using COMSOL Multiphysics software, and the results were compared with the measured 2D RCS.

As a result of this study, the clutter contribution of each sample can be characterized by its 2D RCS. The GTRI focus beam system, a system designed for free-space

material properties measurements, can accurately measure the 2D scattering parameters of data-linked string samples. Due to the thin radii associated with the string samples, the scattering parameters are characterized by the low frequency scattering regime of cylinders. The focus beam measurements of the data-linked strings can be used to determine the effective relative permittivity of the string material. Finally, the strings can be modeled, with relative accuracy, as a single wire coated with a dielectric material.

5.2 Future Research

Although the goals of this research were achieved, this study is just the first step. There are numerous opportunities for future research to better understand the scattering properties of the data-linked strings other than the 2D case. The future research includes additional measurements and modeling. From the 2D RCS, the normal 3D RCS can be predicted using equation (5.1),

$$\sigma_{3D} \simeq \sigma_{2D} \frac{2L^2}{\lambda} \tag{5.1}$$

where L is the length of the data-linked string [5]. The accuracy of the predicted RCS can be verified by measuring strings of various lengths in the AFIT anechoic chamber. Other measurements include oblique angle measurements with the focus beam system. Additional modeling includes using the estimated material properties to model the data-linked string as bare wire with an effective surface impedance. This modeling approach is useful when considering oblique angle illumination where traveling surface waves are induced on the string. Also, 3D models of varying string shapes (s-curves, catenary curves, etc.) can be analyzed to determine how the RCS varies from the straight string case. These results can be verified by measuring similar shapes in the AFIT chamber. As a final suggestion, terminating the string ends can be modeled to determine how to reduce their contributions to the RCS.

Bibliography

1. *Users Guide: Theory and Operation of the GTRI Focused Beam System*, 2007.

2. Abramowitz, Milton and Irene A. Stegun (editors). *Handbook of Mathematical Functions with Formulas, Graphs, and Mathematical Tables*. 1972.

3. Arfken, George B. and Hans J. Weber. *Mathematical Methods for Physicists*. Harcourt/Academic Press, 5th edition, 2001.

4. Badr, Y.A., M.S. Aly, M.F. Hassan, A.M. Elmahdy, and A.M. Azzam. "Far field scattering of Gaussian beam by an infinitely long conducting circular cylinder". *Teaching Photonics at Egyptian Engineering Faculties and Institutes, 2000. Second Workshop on*, 68–83, 2000.

5. Balanis, Constantine A. *Advanced Engineering Electromagnetics*. John Wiley and Sons, 1989.

6. Blacksmith, Jr., P., R.E. Hiatt, and R.B. Mack. "Introduction to radar cross-section measurements". *Proceedings of the IEEE*, 53(8):901–920, Aug. 1965. ISSN 0018-9219.

7. Burns, J. and M. Ricoy. "Investigation of target-support interactions for foam column supports". *Antennas and Propagation Society International Symposium, 1993. AP-S. Digest*, 1796–1799 vol.3, Jun- 2 Jul 1993.

8. Burns, J.W. "Mitigation of target support contamination using an adaptive decomposition technique". *Antennas and Propagation Society International Symposium, 1998. IEEE*, 3:1570–1573 vol.3, Jun 1998.

9. Burns, J.W., G.G. Fliss, and D. Kletzli. "Modeling and measurement of target-string interactions". *Antennas and Propagation Society International Symposium, 1996. AP-S. Digest*, 1:200–203 vol.1, Jul 1996.

10. Chatterjee, A., J.L. Volakis, and W.J. Kent. "Scattering by a perfectly conducting and a coated thin wire using a physical basis model". *Antennas and Propagation, IEEE Transactions on*, 40(7):761–769, Jul 1992. ISSN 0018-926X.

11. Collins, Peter J. "EENG 634 Computational Methods in Electromagnetics Class Notes", Jan 2008. EENG 634 Computational Methods in Electromagnetics.

12. Dybdal, R.B. "Radar cross section measurements". *Proceedings of the IEEE*, 75(4):498–516, April 1987. ISSN 0018-9219.

13. Glaser, J.I. "Some results in the bistatic radar cross section (RCS) of complex objects". *Proceedings of the IEEE*, 77(5):639–648, May 1989. ISSN 0018-9219.

14. Jin, Jianming. *The Finite Element Method in Electromagnetics*. John Wiley and Sons, 2nd edition, 2002.

15. Kent, William J. *Plane Wave Scattering by Thin Linear Dielectric-Coated Wires and Dielectric Strips: A Moment Method Approach with Physical Basis Functions*. Ph.D. thesis, The Ohio State University, 1985.

16. Knott, E. F., J. F. Shaeffer, and M. T. Tuley. *Radar Cross Section*. The SciTech Radar and Defense Series. SciTech Publishing, Inc, Raleigh, NC 27613, 2nd edition, 2004. ISBN 1-891121-25-1. URL `www.scitechpub.com`.

17. Kouyoumjian, R. G. and Jr. L. Peters. "Range Requirements in Radar Cross-Section Measurements". *Proceedings of the IEEE*, 53(8):920–921, Aug. 1965. ISSN 0018-9219.

18. Leon, Steven J. *Linear Algebra with Applications*. Prentice Hall, Inc, 5th edition, 1998.

19. Leon-Garcia, Alberto. *Probability and Random Processes for Electrical Engineers*. Addison-Wesley Publishing Company, Inc, 2nd edition, 1994.

20. Lin, Chi-Sen and M.T. Yaqoob. "A moment method solution for scattering from a dielectrically coated conducting cylinder". *Antennas and Propagation Society International Symposium, 1992. AP-S. 1992 Digest. Held in Conjuction with: URSI Radio Science Meeting and Nuclear EMP Meeting., IEEE*, 777–780 vol.2, Jul 1992.

21. Moore, J. and M.A. West. "Simplified analysis of coated wire antennas and scatterers". *Microwaves, Antennas and Propagation, IEE Proceedings* -, 142(1):14–18, Feb 1995. ISSN 1350-2417.

22. Petersson, L.E.R. and G.S. Smith. "An estimate of the error caused by the plane-wave approximation in free-space dielectric measurement systems". *Antennas and Propagation, IEEE Transactions on*, 50(6):878–887, Jun 2002. ISSN 0018-926X.

23. Swarner, W. and Jr. Peters, L. "Radar cross sections of dielectric or plasma coated conducting spheres and circular cylinders". *Antennas and Propagation, IEEE Transactions on*, 11(5):558–569, Sep 1963. ISSN 0018-926X.

24. Tezel, N.S. and S. Paker. "Bi-static radar cross section (RCS) reduction of impedance cylinder". *Radar, 2006 IEEE Conference on*, 4 pp.–, April 2006.

25. Van, T., J. Berrie, K. Hill, and G. Simpson. "Numerical Analysis of the Focused-Beam Measurement System". Antenna Measurements Technique Association, October 2004.

26. Wei, P. and A. Reed. "Interference of a long dielectric string with a short metallic wire in RCS measurements". *Antennas and Propagation Magazine, IEEE*, 50(1):233–239, Feb. 2008. ISSN 1045-9243.

27. Willis, Nicholas J. *Bistatic Radar*. SciTech Publishing, 2nd edition, 2005.

REPORT DOCUMENTATION PAGE

Form Approved
OMB No. 0704–0188

1. REPORT DATE *(DD–MM–YYYY)*	2. REPORT TYPE	3. DATES COVERED *(From — To)*
26–03–2009	Master's Thesis	Sept 2007 — Mar 2009

4. TITLE AND SUBTITLE

Two Dimensional Scattering Analysis of Data-Linked Support Strings for Bistatic Measurement Systems

5a. CONTRACT NUMBER

5b. GRANT NUMBER

5c. PROGRAM ELEMENT NUMBER

6. AUTHOR(S)

William Keichel, Capt, USAF

5d. PROJECT NUMBER

08-217

5e. TASK NUMBER

5f. WORK UNIT NUMBER

7. PERFORMING ORGANIZATION NAME(S) AND ADDRESS(ES)

Air Force Institute of Technology
Graduate School of Engineering and Management (AFIT/EN)
2950 Hobson Way
WPAFB OH 45433-7765

8. PERFORMING ORGANIZATION REPORT NUMBER

AFIT/GE/ENG/09-24

9. SPONSORING / MONITORING AGENCY NAME(S) AND ADDRESS(ES)

AFRL/RYS (Dr. Byron Welsh)
2591 K St.
Area B, Bldg 254
Wright-Patterson Air Force Base, OH 45433
((937) 255-7184 byron.welsh@wpafb.af.mil)

10. SPONSOR/MONITOR'S ACRONYM(S)

AFRL/RYS

11. SPONSOR/MONITOR'S REPORT NUMBER(S)

12. DISTRIBUTION / AVAILABILITY STATEMENT

Approval for public release; distribution is unlimited.

13. SUPPLEMENTARY NOTES

14. ABSTRACT

Use of data-linked strings to support a bistatic antenna is being considered as a possible improvement to indoor bistatic radar cross section measurement systems. Analysis of candidate data-linked strings is required to understand the potential clutter contribution posed by such a system. The main objective of this research is to determine the scattering properties of four data-linked support string samples. Another goal is to determine the material properties of the string material through nondestructive means if possible. The final goal is to model the samples as a single wire coated with a dielectric material and determine the validity of the model. To meet these goals, the two dimensional radar cross section of each sample is measured with a focused beam system. The resulting measurements are used in conjunction with an analytic model of a dielectric-coated wire to estimate the material properties of the string material. Finally, a dielectric-coated wire model for each sample is analyzed using COMSOL Multiphysics software, and the results are compared with the measured two dimensional radar cross section.

15. SUBJECT TERMS

RCS, 2D RCS, Bistatic RCS, Focus-Beam System

16. SECURITY CLASSIFICATION OF:			17. LIMITATION OF ABSTRACT	18. NUMBER OF PAGES	19a. NAME OF RESPONSIBLE PERSON
a. REPORT	b. ABSTRACT	c. THIS PAGE			Dr. Peter Collins
U	U	U	UU	80	19b. TELEPHONE NUMBER *(include area code)* (937) 255–3636, ext 7256; peter.collins@afit.edu